The Astrophysical Journal, 1007:67 (21pp), 2026 August 10 https://doi.org/10.3847/1538-4357/ae8760

Properties of Black Hole Mergers in Disks of Active Galactic Nuclei

Hiromichi Tagawa[1], Zoltán Haiman[2,3,4], and Bence Kocsis[5,6]
[1] Shanghai Astronomical Observatory, Shanghai 200030, People's Republic of China; htagawa@shao.ac.jp
[2] Institute of Science and Technology Austria, Am Campus 1, Klosterneuburg 3400, Austria
[3] Department of Astronomy, Columbia University, 550 West 120th Street, New York, NY 10027, USA
[4] Department of Physics, Columbia University, 550 West 120th Street, New York, NY 10027, USA
[5] Rudolf Peierls Centre for Theoretical Physics, University of Oxford, Clarendon Laboratory, Parks Road, Oxford OX1 3PU, UK
[6] St Hugh's College, University of Oxford, St Margaret's Road, Oxford OX2 6LE, UK
Received 2026 April 28; revised 2026 June 12; accepted 2026 July 3; published 2026 August 6

Abstract

Ground-based gravitational-wave (GW) observatories have detected approximately 200 binary black hole (BH) mergers. The astrophysical origin of these events is debated, with evidence suggesting that at least a subset originated from dynamic environments characterized by frequent close encounters. Accretion disks in active galactic nuclei (AGNs) are of particular interest, as certain observed features could be more readily produced within such environments. In this paper, we investigate the expected properties of mergers in these environments, and their dependence on various parameters, using 1D *N*-body simulations combined with a comprehensive semianalytical model. In our fiducial model, the distributions of masses (m_1 and m_2) and mass ratios ($q \equiv m_2/m_1 \leqslant 1$) are similar to those observed. However, they depend strongly on the lifetime and density of the AGN disk and on the number and accretion efficiency of BHs, with higher masses predicted as these quantities increase. The most massive mergers, such as GW231123, can be produced either by efficient gas accretion or by hierarchical mergers among $\geqslant$3 generations of BHs. The observed negative correlation between q and the average effective spin ($\chi_{\rm eff}$), along with the positive correlation between $\chi_{\rm eff}$ and the chirp mass ($M_{\rm chirp}$), can be explained by a combination of efficient gas accretion, which promotes spin alignment, and hierarchical mergers, which produce high-$|\chi_{\rm eff}|$ and low-q binaries. Hierarchical mergers can also explain the negative correlation between q and the dispersion of $\chi_{\rm eff}$, as well as the positive correlation between $|\chi_{\rm eff}|$and $M_{\rm chirp}$. We present a comprehensive study on how the expected distribution of each of these quantities depends on model parameters and assumptions, which will aid the interpretation of observed GW population properties.

Unified Astronomy Thesaurus concepts: Gravitational wave sources (677); Astrophysical black holes (98); Active galactic nuclei (16); Accretion (14)

1. Introduction

Gravitational waves (GWs) from approximately 200 mergers among black holes (BHs) and neutron stars (NS; The LIGO Scientific Collaboration et al. 2026a, 2026b) have been detected by LIGO (LIGO Scientific Collaboration et al. 2015), Virgo (F. Acernese et al. 2015), and KAGRA (T. Akutsu et al. 2021). An outstanding question is the astrophysical pathway(s) leading to these mergers, which remain(s) highly debated. Promising channels for their formation include isolated binary evolution (e.g., M. Dominik et al. 2012; T. Kinugawa et al. 2014; K. Belczynski et al. 2016; M. Spera et al. 2019; A. Tanikawa et al. 2022; F. Kıroğlu et al. 2025a, 2025b), the evolution of triple or quadruple systems (e.g., F. Antonini et al. 2017; K. Silsbee & S. Tremaine 2017; G. Fragione & B. Kocsis 2019), dynamical evolution within star clusters (e.g., S. F. Portegies Zwart & S. L. W. McMillan 2000; J. Samsing et al. 2014; R. M. O'Leary et al. 2016; C. L. Rodriguez et al. 2016; S. Banerjee 2017; J. Samsing & E. Ramirez-Ruiz 2017; B.-M. Hoang et al. 2018; G. Fragione et al. 2019; J. Kumamoto et al. 2019; A. Rasskazov & B. Kocsis 2019; S. Rastello et al. 2019; M. Arca Sedda 2020), and in disks of active galactic nuclei (AGNs; e.g., I. Bartos et al. 2017b; N. C. Stone et al. 2017; B. McKernan et al. 2018; H. Tagawa et al. 2020c).

Dynamical channels can explain many of the unusual features reported for several detections. One distinguishing property is the eccentricity of merging binaries. High eccentricity has been suggested for at least one of the proposed GW events (V. Gayathri et al. 2022; I. Romero-Shaw et al. 2022; N. Gupte et al. 2025, 2026; M. d. L. Planas et al. 2025; I. Romero-Shaw et al. 2025; G. Morras et al. 2026; Y. Xu et al. 2026). Such eccentricity is typically expected in mergers occurring within dynamical environments (F. Antonini et al. 2018; C. L. Rodriguez & F. Antonini 2018; K. Kremer et al. 2020; H. Tagawa et al. 2021b; M. Zevin et al. 2021; I. Romero-Shaw et al. 2025). Another significant discovery is that of unusually massive BHs. Events like GW190521 (R. Abbott et al. 2020) and GW231123 (A. G. Abac et al. 2025a) are notably massive, posing challenges for formation through isolated binary evolution (J. Stegmann et al. 2025; A. Tanikawa et al. 2026) due to the mass gap associated with pair-instability supernovae (E. Chatzopoulos & J. C. Wheeler 2012; see also D. Croon et al. 2026). Additionally, GW190521 suggests either strong precession or high eccentricity (I. Romero-Shaw et al. 2020; V. Gayathri et al. 2022; R. Gamba et al. 2023; I. M. Romero-Shaw et al. 2023), phenomena difficult to produce through isolated channels, but more naturally arising in dynamical channels.

Globular clusters are known to be important sites for the dynamical BH merger channel due to their high density and low velocity dispersion, which lead to high scattering cross sections for binary formation and evolution. However, the total mass of globular clusters within a galaxy is roughly comparable to that of nuclear star clusters (M. Arca-Sedda & R. Capuzzo-Dolcetta 2014; K. Fahrion et al. 2022), particularly in abundant galaxies with stellar masses of $\lesssim 10^{11}\,M_\odot$ (P. Madau & M. Dickinson 2014). This similarity suggests that the number of BHs in both environments may be comparable. Therefore, the efficiency of mergers in each environment is crucial in determining their relative contributions to GW events. While the number densities in nuclear star clusters can greatly surpass those in globular clusters at their centers, the velocity dispersion due to the central supermassive BH (SMBH) is also much larger, and dynamical binary formation scales with $\rho^3 v^{-9}$ (e.g., S. J. Aarseth & D. C. Heggie 1976; J. Binney & S. Tremaine 2008). This indicates that binary formation is more efficient in globular clusters during gasless phases. On the other hand, during active phases when dense disks are present, H. Tagawa et al. (2020c) showed that binary formation and hierarchical mergers are frequent in nuclear star clusters. If mergers predominantly occur in galactic centers, K. E. S. Ford & B. McKernan (2022) argued that mergers during active phases surpass those during quiescent phases, as interactions with gas enhance the merger rate enormously. Consequently, a significant number of mergers could be expected to occur within AGN disks.

A potential signature of mergers in AGN disks is electromagnetic counterparts. Recent observations suggest that gamma-ray (but see Z. Bagoly et al. 2016; V. Connaughton et al. 2016; J. DeLaunay et al. 2024; S.-R. Zhang et al. 2026) and optical flares (M. J. Graham et al. 2020, 2023) may be associated with GW events. These associations can be attributed to emission from merging BHs in AGN disks (B. McKernan et al. 2019; H. Tagawa et al. 2023a, 2023b; K. Chen & Z.-G. Dai 2024, 2025; J. C. Rodríguez-Ramírez et al. 2024, 2025; Z.-P. Ma et al. 2025; H. Tagawa et al. 2026a). If these associations are genuine (V. Connaughton et al. 2018; G. Ashton et al. 2021; J. Calderón Bustillo et al. 2021; A. Palmese et al. 2021; S. L. Morton et al. 2023; N. Veronesi et al. 2025a), they could serve as key signatures of mergers occurring in AGN disks. Another potential signature is the spatial correlation between the (3D) locations of GW events and AGNs (I. Bartos et al. 2017a; K. R. Corley et al. 2019; N. Veronesi et al. 2022, 2023, 2025b; J. W. N. Moncrieff & F. H. Panther 2025). A recent analysis using LIGO–Virgo–KAGRA (LVK) the fourth observing run (O4) data estimated that the fraction of mergers originating from AGNs is ∼0.1–0.8 with a 90% confidence level, excluding high-luminosity ($\geqslant 10^{45}\,\mathrm{erg\,s^{-1}}$) AGNs (L.-G. Zhu & X. Chen 2025). The alignment of BH spins with the orbital angular momentum for massive mergers, especially in the upper-mass gap, may also serve as a potential signature of mergers in AGN disks (Y.-J. Li et al. 2026b). Therefore, there are compelling suggestions that some mergers originate in AGN disks. Given this promising pathway, it would be beneficial to further elucidate how BHs merge in AGN disks and to identify the distribution of the expected properties of these mergers.

In an AGN disk, compact objects (COs), including stellar-mass BHs, are embedded through capture via dynamical interactions between the nuclear star cluster and the AGN disk (J. P. Ostriker 1983; D. Syer et al. 1991; I. Bartos et al. 2017b; B. McKernan et al. 2018; A. Generozov & H. B. Perets 2023; Y. Wang et al. 2024; C. Rowan et al. 2025a; H. Whitehead et al. 2025). Additionally, stars form in outer regions of the AGN disk where the self-gravity of gas becomes significant, contributing to the presence of COs in the disk (Y. Levin & A. M. Beloborodov 2003; J. Goodman & J. C. Tan 2004; M. Milosavljević & A. Loeb 2004; T. A. Thompson et al. 2005; S. Nayakshin et al. 2007; N. C. Stone et al. 2017; S. Gilbaum & N. C. Stone 2022; Y.-X. Chen et al. 2023; A. Derdzinski & L. Mayer 2023; M. Epstein-Martin et al. 2025b).

COs in the AGN disk migrate by interacting with the gas disk, and are predicted to accumulate in regions such as migration traps and gap-forming regions (J. M. Bellovary et al. 2016; F. S. Masset 2017; A. M. Derdzinski et al. 2019; A. Secunda et al. 2019, 2020; Y. Yang et al. 2019a, 2019b; A. M. Hankla et al. 2020; H. Tagawa et al. 2020c; Z. Pan & H. Yang 2021a; P. Peng & X. Chen 2021; E. Grishin et al. 2024; M. P. Vaccaro et al. 2024; M. Epstein-Martin et al. 2025a; S. Gilbaum et al. 2025; L. Xue et al. 2025; J. W. N. Moncrieff et al. 2026; L. Xue et al. 2026). Within these regions, they efficiently encounter one another and form binaries under the influence of gaseous torques (P. Goldreich et al. 2002; A. Secunda et al. 2019, 2020; H. Tagawa et al. 2020c; J. Li et al. 2022a; S. DeLaurentiis et al. 2023; C. Rowan et al. 2023, 2024; M. Rozner et al. 2023; M. Dodici & S. Tremaine 2024; K. Qian et al. 2024; H. Whitehead et al. 2024a, 2024b) and GW emission (H. Tagawa et al. 2021b; J. Samsing et al. 2022; T. C. N. Boekholt et al. 2023; J. Li et al. 2023). After their formation, these binaries are hardened (or softened) by gaseous torques (M. Gröbner et al. 2020; Y.-P. Li et al. 2021, 2022c, 2022b; Y.-X. Chen et al. 2022; A. M. Dempsey et al. 2022; R. Li & D. Lai 2022, 2023, 2024; J. Calcino et al. 2024; A. J. Dittmann et al. 2024, 2025; W. Ishibashi & M. Gröbner 2024; C. Rowan et al. 2024, 2025b; M. Rozner & H. B. Perets 2024; H. Whitehead et al. 2025) and by binary–single interactions (D. C. Heggie 1975; N. W. C. Leigh et al. 2018; H. Tagawa et al. 2020c; Y. B. Ginat & H. B. Perets 2021, 2023; J. Samsing et al. 2022; C. Rowan et al. 2025c; Y. Su et al. 2025; M. Wang et al. 2025a, 2025b; L. Xue et al. 2025), before GW emission (P. C. Peters 1964) drives them to merge.

Several groups have studied the evolution of a population of BHs in AGN disks using Monte Carlo–like methods. B. McKernan et al. (2020, 2025), H. E. Cook et al. (2025), and V. Delfavero et al. (2025) investigated the properties of mergers occurring in both migration traps and other locations, while simplifying many processes (see Section 3.1.4). Y. Yang et al. (2019a, 2019b), and M. P. Vaccaro et al. (2024) focused specifically on the properties of mergers within migration traps. Our models focus on mergers outside migration traps and, for the first time, incorporate binary formation via gaseous torques and three-body interactions (H. Tagawa et al. 2020c), GW capture (GWC) processes (H. Tagawa et al. 2021b), binary–single interactions (H. Tagawa et al. 2021c), the effects of kicks due to mergers and interactions, gap formation (with an updated prescription), as well as the evolution of spin and binary angular momentum due to gas accretion (H. Tagawa et al. 2020b), to predict the properties of BH mergers in AGN disks.

We found that most BH mergers occur in the inner regions, where gaps often form and binary–single interactions significantly facilitate mergers (H. Tagawa et al. 2020c). Consequently, the mass ratio for the merging binaries is predicted to be close to unity (V. Gayathri et al. 2021), and the effective spin parameter is distributed around zero (H. Tagawa et al. 2020b). Moreover, the merging masses are characterized by frequent hierarchical mergers, due to the high escape velocity from the gravitational potential of the SMBH (H. Tagawa et al. 2021c). Comparisons between observed BH masses, spins, and merger rates suggest that a substantial fraction of the observed mergers may indeed originate in AGN disks (V. Gayathri et al. 2021; H. Tagawa et al. 2021c; K. E. S. Ford & B. McKernan 2022; B. McKernan et al. 2025). It is also suggested that various parameters and processes, such as migration (E. Grishin et al. 2024), interactions (A. A. Trani et al. 2024), eccentricity (J. Samsing et al. 2022), and accretion (M. C. Begelman & M. Volonteri 2017; Z. Roupas 2025, 2026) , may affect the distributions of observables.

In this paper, we investigate the expected properties of mergers in these environments and their dependence on various parameters, using 1D N-body simulations combined with a semianalytical model. We have updated and varied the prescriptions for encounters, interactions, migration, accretion onto BHs, and AGN structures. Additionally, we explore the impact of key parameters, including AGN duration, BH number density, SMBH mass, and the accretion rate onto the SMBH. We compare the predicted properties of BH mergers with observations from LVK and discuss the parameter space in which the AGN channel could significantly contribute to the observed events.

This paper is organized as follows: in Section 2, we detail the methods used in our models, Section 3 presents our main findings, and Section 4 summarizes our key conclusions.

2. Methods

2.1. Overview of Models

We utilize the models employed in H. Tagawa et al. (2021c), which track N-body particles representing BHs. Here, we provide an overview of the processes involved in the evolution and mergers of BHs in an AGN disk in this model.

Disk model. For the AGN accretion disk we assume a flat, geometrically thin, optically thick, radiatively efficient, N. I. Shakura & R. A. Sunyaev (1973) model assuming local thermal equilibrium between viscous heating and radiative cooling. The model is extended into the outer gravitationally unstable region assuming $Q = 1$ Toomre parameter due to star formation following T. A. Thompson et al. (2005, hereafter TQM) in our fiducial model, where the opacity model is given by K. R. Bell & D. N. C. Lin (1994). We use a stationary passive disk model, i.e., the AGN disk properties are not affected by the presence of BHs or the nuclear star cluster during the simulation, neglecting possible feedback effects, and employ analytic prescriptions for accretion, migration, and spin changes independently for all embedded objects using the local physical properties of the disk. Gap formation and its influence are taken into account, reflecting the individual BH mass; for simplicity, the gap depth is assumed to be unaffected by other BHs orbiting in the same annulus.[7] We assume that the efficiency of angular momentum transport due to global gravitational torques in the outer regions is $m_{\rm AM} = 0.15$ (TQM). The outer boundary from which gas inflows is set at $r_{\rm out} = 5$ pc, the pressure ratio parameter is assumed to be $\xi = 1$, and the conversion efficiency of star formation to radiation is $\epsilon = 1.5 \times 10^{-4}$ (TQM). In the inner regions, the efficiency due to local viscous torque is $\alpha_{\rm SS} = 0.1$ (N. I. Shakura & R. A. Sunyaev 1973). In the transition between the inner and outer regions, the degree of angular momentum transport is adjusted to keep $Q = 1$. This transition is based on the consideration that the mechanisms for angular momentum transfer likely differ depending on location (TQM; S. Collin & J.-P. Zahn 2008). We also investigate cases where viscosity is prescribed uniformly (see Section 2.2 below).

BH processes. Initially, BHs reside within the nuclear star cluster surrounding the SMBH (J. Miralda-Escudé & J. A. Kollmeier 2005; T. Alexander & C. Hopman 2009; R. M. O'Leary et al. 2009; A. Rasskazov & B. Kocsis 2019). We assume that the initial density distribution of all BHs is slightly steeper than the single-mass Bahcall–Wolf distribution by 0.25 in the power-law index, which is suggested by numerical simulations (e.g., M. Freitag et al. 2006; C. Hopman & T. Alexander 2006; R. M. O'Leary et al. 2009). These BHs are gradually captured by the AGN disk through accretion torques and gas dynamical friction (Y. Wang et al. 2024). BHs can also form in the outer regions of the AGN disk, where the gas becomes gravitationally unstable (TQM; M. Epstein-Martin et al. 2025b).

Within the AGN disk, BHs migrate toward the SMBH due to type I and II torques exerted by the AGN disk (e.g., S. Gilbaum et al. 2025), and binaries form through gas dynamical friction during two-body encounters (P. Goldreich et al. 2002) as well as through dynamical interactions during three-body encounters (e.g., S. J. Aarseth & D. C. Heggie 1976). After their formation, the angular momentum of these binaries evolves due to gas dynamical friction and torques from circumsingle and circumbinary disks (I. Bartos et al. 2017b). Additionally, binaries can interact with single stars, other BHs, and other BH binaries. Following binary–single (or binary–binary) interactions, the semimajor axes and velocities of the binaries evolve, as described in N. W. C. Leigh et al. (2018), and we assume that the directions of the orbital angular momenta are randomized, and the eccentricity distribution is thermalized. The two most massive BHs are assumed to remain as binary components after binary–single and binary–binary interactions. The velocities of all BHs evolve due to scattering with other objects (J. Binney & S. Tremaine 2008). Highly eccentric BH binaries can also form via GWC in single–single encounters (e.g., R. M. O'Leary et al. 2009) or through binary–single interactions (J. Samsing et al. 2014; H. Tagawa et al. 2021b).

In later phases, the semimajor axes and eccentricities of the binaries decrease due to GW emission (P. C. Peters 1964). When the pericenter distance of a binary becomes smaller than the innermost stable orbit, we assume that the BHs merge, assigning a kick velocity (C. O. Lousto et al. 2012), accounting for mass loss due to GW emission (E. Barausse et al. 2012), and modeling the spin evolution at merger (L. Rezzolla et al. 2008). BH masses and spins grow through mergers and Eddington-limited accretion (H. Tagawa et al. 2020b).

2.2. Updates

Radiative feedback. L. Xue et al. (2025) performed semianalytic simulations that adopt physical prescriptions

[7] According to our test calculations, in which the gap depth is determined by the most massive BH in each grid, this simplified prescription has a moderate effect on the merging-mass distribution. The number of mergers at $t = 3$ Myr and the top 1% masses among merging binaries among 10 simulations are 2×10^3 and 220 $M_\odot$, respectively. We find there are no noticeable differences in the observable properties resulting from this change.

similar to those in H. Tagawa et al. (2020c), while treating the evolution of background objects in a probabilistic manner. By comparing the results of L. Xue et al. (2025), we found that radiative feedback was not effectively considered in H. Tagawa et al. (2020c) due to computational bugs (mistakes in unit conversion). To address this oversight, we turn off gas dynamical friction when specific conditions are met (Section 3.3 in H. Tagawa et al. 2020c). In such cases, the gas-capture rate by the BH is capped at the Eddington rate, and the accretion drag reduces due to the decreased capture rate.

Dynamical encounter probabilities. In H. Tagawa et al. (2020c), the encounter probabilities for several mechanisms—such as gas-capture binary formation, three-body binary formation, GWC binary formation, and binary–single interactions—were overestimated. The local two-body encounter timescale is given by $t_{\rm enc,local} = 1/(n\sigma v)$, where n is the number density of BHs in the AGN disk, $\sigma = \Delta z\Delta r$ is the encounter cross section, v is the relative velocity between BHs, and Δr and Δz are, respectively, the radial and vertical scales over which encounters can occur, influenced by several factors including the tidal force from the SMBH. Their specific values are provided in Sections 3.3.5, 3.3.7, and 3.3.8 in H. Tagawa et al. (2020c) and Section 2.2.1 in H. Tagawa et al. (2021b) for binary–single interactions, three-body binary formation, gas-capture binary formation, and GWC binary formation, respectively. Here, v is taken as the maximum of the migration, shear, and random velocities from our previous studies (e.g., H. Tagawa et al. 2020c). However, this expression for the timescale is valid only when more than one BH resides within annuli within Δr from one another, $N_{\Delta r} = 2\pi rn\sigma > 1$. In other cases, the timescale for migration into an annulus containing other BHs also needs to be considered. Thus, the encounter timescale is given as the maximum of (i) the above local encounter timescale ($t_{\rm enc,local}$) and (ii) the migration timescale to reach an annulus containing another BH, given by $t_{\rm mig-BH} = 1/2\pi r\Delta z n v_{\rm mig,rel}$, where $v_{\rm rel,mig}$ is the relative migration velocity of the BH with respect to another BH, considering gap formation (H. Tagawa et al. 2020c). Furthermore, if the crossing timescale within Δr, given by $t_{\rm cross} = \Delta r/v_{\rm mig,rel}$, is shorter than the encounter timescale ($t_{\rm enc,local}$), then BHs needs to cross $N_{\rm cross} = t_{\rm enc,local}/t_{\rm cross}$ annuli containing BHs for an encounter to occur. Therefore, the total encounter timescale is expressed as

$$t_{\rm enc} = \begin{cases} t_{\rm enc,local} \quad \text{for } N_{\Delta r} \geqslant 1, \\ \max(t_{\rm enc,local},\, t_{\rm mig-BH}) \\ \text{for } N_{\Delta r} < 1 \text{ and } t_{\rm cross} > t_{\rm enc,local}, \\ \max(t_{\rm enc,local},\, N_{\rm cross} t_{\rm mig-BH}) \\ \text{for } N_{\Delta r} < 1 \text{ and } t_{\rm cross} < t_{\rm enc,local}. \end{cases} \quad (1)$$

In this way, this prescription for the encounter timescale is updated for gas-capture binary formation, three-body binary formation, GWC binary formation, and binary–single interactions.

Exchange interactions. We also discovered that the exchange of binary components, as implemented in H. Tagawa et al. (2021c), was not functioning correctly (as spin values were occasionally not properly conserved), and we have corrected this bug.

Accretion rate. In our fiducial model, the accretion rate onto the SMBH is reduced to 0.01 times the Eddington rate, compared to 0.1 times the Eddington rate used in H. Tagawa et al. (2020c). This change reflects the findings that most mergers likely originate from lower-luminosity AGNs (H. Tagawa et al. 2020c), given their abundance (J. E. Greene & L. C. Ho 2007) and the weak dependence of the merger rate on the accretion rate, as long as thin disks form around the SMBH (C. Rowan et al. 2025b; H. Whitehead et al. 2025). Consequently, models with low accretion rates onto SMBHs should be more common among BH mergers in AGNs.

BH mass distribution. While the upper-mass limit for first-generation BHs in H. Tagawa et al. (2020c) is set to $15\,M_\odot$, motivated by the supersolar metallicity of stars in the Galactic center (T. Do et al. 2018), we adopt a model in which the BH mass is multiplied by a factor of 2, as prescribed in H. Tagawa et al. (2021c). This adjustment accounts for the lower metallicity in nuclear star clusters around lower-mass SMBHs (K. Fahrion et al. 2021), which are likely formed through the accretion of globular clusters (M. Arca-Sedda & R. Capuzzo--Dolcetta 2014; K. Fahrion et al. 2022). Moreover, high initial BH masses are required to account for the change in spin magnitude at high masses through the AGN channel (see Section 3.1.4).

To reduce computational costs, we focus solely on the evolution of BHs and stars, excluding NSs, unlike in H. Tagawa et al. (2021c).

Natal BH spin. Based on the distribution of BH spin magnitudes inferred from the LVK observations (C. Adamcewicz et al. 2025; The LIGO Scientific Collaboration et al. 2026b; N. Guttman et al. 2026), we adopt a natal spin magnitude of $a = 0.1$, instead of $a = 0$ used in our previous works.

Inner boundary. Finally, we adjusted the inner radius for BH removal from 10^{-4} to 10^{-6} pc to ensure that we do not miss mergers occurring close to the SMBH.

The parameters of our fiducial model (M1) are listed in Table 1, which are consistent with those in H. Tagawa et al. (2021c), except for the aforementioned adjustments.

2.3. Model Variation

To understand the parameter dependence of observables, we have performed simulations using 20 models, labeled M1–M20. Model M1 corresponds to the fiducial model (Table 1), while the parameters or prescriptions are varied in models M2–M20 (Table 2).

Velocity dispersion. In model M2, the velocity dispersion of BHs follows an isotropic distribution, and β_v is not used. Note that the isotropic distribution differs from the Gaussian distribution adopted in the fiducial model, and stars typically have higher inclination angles (see L. Xue et al. 2025). In model M3, the velocity dispersion of BHs is increased to $\beta_v = 1$, where $\beta_v v_{\rm kep}(r)$ represents the BH velocity dispersion and $v_{\rm kep}(r)$ is the Keplerian velocity at distance r from the SMBH.

BH numbers. In model M4, the initial number of BHs is reduced from $N_{\rm BH,ini} = 2\times10^4$ to 7×10^3.

Geometry: 2D model. In model M5, binary–single interactions are assumed to occur in a 2D geometry, coplanar with the AGN disk (J. Samsing et al. 2022; H. Tagawa et al. 2021b).

SMBH mass. In model M6, the SMBH mass is increased to $M_{\rm SMBH} = 4\times10^7\,M_\odot$.

Accretion rate. In model M7, the gas inflow rate at the outer radius of the simulation is set to be $\dot{M}_{\rm out} = 0.1\dot{M}_{\rm Edd}(M_{\rm SMBH})$ to investigate the dependence on the gas inflow rate, where $\dot{M}_{\rm Edd}(M)$ is the Eddington accretion rate onto a BH of mass M.

Table 1
Fiducial Values of Our Model Parameters

Parameter	Fiducial Value	References
Spatial directions in which binary–single interactions occur	Isotropic in 3D	H. Tagawa et al. (2021b), J. Samsing et al. (2022)
Number of temporary binary BHs formed during a binary–single interaction	$N_{\rm int} = 20$	J. Samsing et al. (2014)
Initial BH spin magnitude	$\|\boldsymbol{a}\| = 0.1$	The LIGO Scientific Collaboration et al. (2026b)
Angular momentum directions of circum-BH disks	$\hat{\boldsymbol{J}}_{\rm CBHD} = \hat{\boldsymbol{J}}_{\rm AGN}$ for single BHs, $\hat{\boldsymbol{J}}_{\rm CBHD} = \hat{\boldsymbol{J}}_{\rm bin}$ for BHs in binaries	e.g., S. H. Lubow et al. (1999), M. S. L. Moody et al. (2019)
Ratio of viscosity responsible for warp propagation over that for transferring angular momentum	$\nu_2/\nu_1 = 10$	G. I. Ogilvie (1999), G. Lodato & D. Gerosa (2013)
Alignment efficiency of the binary orbital angular momentum due to gas capture	$f_{\rm rot} = 1$ (Equation (14) in H. Tagawa et al. 2020b)	A. J. Dittmann et al. (2024), G. Fabj et al. (2026)
Mass of the central SMBH	$M_{\rm SMBH} = 4 \times 10^6\,M_\odot$	A. M. Ghez et al. (2008), R. Genzel et al. (2010)
Gas accretion rate at the outer radius of the simulation (5 pc)	$\dot{M}_{\rm out} = 0.01\dot{M}_{\rm Edd}$ with $\eta = 0.1$	J. E. Greene & L. C. Ho (2007), H. Tagawa et al. (2020c)
Fraction of preexisting binaries in 3D star cluster	$f_{\rm pre} = 0.15$	O. Pfuhl et al. (2014), A. P. Stephan et al. (2016)
Power-law exponent for the initial density profile for BHs	$\gamma_\rho = 0$	C. Hopman & T. Alexander (2006), R. M. O'Leary et al. (2009)
Initial velocity anisotropy parameter such that $\beta_v v_{\rm kep}(r)$ is the BH velocity dispersion	$\beta_v = 0.2$	S. Yelda et al. (2014), A. Szolgyen & B. Kocsis (2018)
Efficiency of angular momentum transport in the α disk	$\alpha_{\rm SS} = 0.1$	A. R. King et al. (2007)
Stellar mass within 3 pc	$M_{\rm star,3pc} = 10^7\,M_\odot$	A. Feldmeier et al. (2014), R. Schödel et al. (2014)
Stellar initial mass function slope	$\delta_{\rm IMF} = 2.35$	H. Bartko et al. (2010), J. R. Lu et al. (2013)
Angular momentum transfer parameter in the outer star-forming regions	$m_{\rm AM} = 0.15$ (Equation C8 in TQM)	TQM, S. Collin & J.-P. Zahn (2008)
Accretion rate in Eddington units onto stellar-mass BHs with a radiative efficiency $\eta = 0.1$	$\Gamma_{\rm Edd,cir} = 1$	e.g., P. C. Fragile et al. (2025)
Numerical time-step parameter	$\eta_t = 0.1$	H. Tagawa et al. (2020c)
Number of radial cells storing physical quantities	$N_{\rm cell} = 120$	H. Tagawa et al. (2020c)
Minimum and maximum distances from an SMBH for the initial BH distribution	$r_{\rm in,BH} = 10^{-6}$ pc, $r_{\rm out,BH} = 3$ pc	A. Feldmeier et al. (2014)
Initial number of BHs within 3 pc from an SMBH	$N_{\rm BH,ini} = 2 \times 10^4$	H. Bartko et al. (2010), J. R. Lu et al. (2013)

BH masses. In model M8, the initial BH mass is multiplied by 3/2 relative to the fiducial model, resulting in maximum BH masses of 45 $M_\odot$, considering mass gaps caused by pair-instability supernovae (e.g., S. E. Woosley & A. Heger 2021).

Migration. In model M9, BHs do not migrate within the AGN disk. In model M10, thermal torque is included to calculate migration (E. Grishin et al. 2024).

Radiation feedback. In model M11, the effects of radiation feedback on gaseous torques are turned off, to examine the case effectively prescribed in H. Tagawa et al. (2020c) due to a bug.

Binary–single interactions. In model M12, the orbital angular momentum directions of binaries are assumed to be unaffected by binary–single interactions, while the semimajor axis and eccentricity are influenced in the same way as in the fiducial model. This represents an extreme case of inefficient randomization suggested by A. A. Trani et al. (2024) and G. Fabj et al. (2026).

AGN model. In models M13 and M14, the AGN disk model proposed by SG is employed, with the accretion rates onto the SMBH set to $\dot{M}_{\rm SMBH} = 0.1\dot{M}_{\rm Edd}(M_{\rm SMBH})$ and $0.01\dot{M}_{\rm Edd}(M_{\rm SMBH})$, respectively. In models M15 and M16, the AGN disk model proposed by TQM is utilized with $\dot{M}_{\rm SMBH} = 0.1\dot{M}_{\rm Edd}(M_{\rm SMBH})$ and $0.01\dot{M}_{\rm Edd}(M_{\rm SMBH})$, respectively. The parameters in models M13–M16 are set to the fiducial values in D. Gangardt et al. (2024). In the models M15 and M16, the efficient angular momentum parameter is applied across all regions including the inner regions, which differs from the fiducial model (Section 2.1, Figure 1).

BH accretion. In models M17–M20, we modify the prescriptions for accretion onto BHs. In models M17 and M18, the accretion rate onto a BH is given by

$$\dot{M}_{\rm BH} = \dot{M}_{\rm BHL}\left(\frac{r_{\rm in}}{r_{\rm wind}}\right)^s, \quad (2)$$

where $r_{\rm wind}$ and $r_{\rm in}$ are the radii inside and outside of which wind mass loss becomes significant, respectively, and $\dot{M}_{\rm BHL}$ is the gas-capture rate by the BH (H. Tagawa et al. 2020c; see also N. Kaaz et al. 2023). The inflow rate decreases with radius following a power law due to wind mass loss, as predicted by adiabatic inflow–outflow solutions (ADIOS; R. D. Blandford & M. C. Begelman 1999), observations (J. Poutanen et al. 2007), and numerical simulations (e.g., H. Hu et al. 2022; P. C. Fragile et al. 2025). We set $r_{\rm in} = 5r_{\rm g}$ (Z. Pan & H. Yang 2021b), where $r_{\rm g}$ is the

Table 2
The Assumptions, Motivation, and Results in Different Models

Input			Output	
Model	Parameter	Motivation of Parameter Search	$N_{\rm mer,10}$	$M_{\rm top1}$ ($M_\odot$)
M1	Fiducial	...	3×10^3	180
M2	Isotropic velocity distribution	Dependence on velocity structure of a nuclear star cluster	10^3	43
M3	$\beta_v = 1$	”	10^3	110
M4	$N_{\rm BH,ini} = 6000$	Dependence on the number of BHs in a nuclear star cluster	8.0×10^2	120
M5	Binary–single interactions in 2D	Influence of aligned interactions (J. Samsing et al. 2022)	6×10^3	350
M6	$M_{\rm SMBH} = 4 \times 10^7\,M_\odot$	Dependence on the SMBH mass	3×10^3	210
M7	$\dot{M}_{\rm out} = 0.1\dot{M}_{\rm Edd}$	Dependence on the AGN inflow rate	4×10^3	560
M8	The initial BH masses are multiplied by 3/2	Dependence on the initial BH mass	3×10^3	220
M9	No migration	Influence of migration	2×10^3	120
M10	With thermal torques	Influence of thermal torques	2×10^3	180
M11	No radiation feedback	Influence of radiation feedback	3×10^3	170
M12	No angular momentum change at binary–single interactions	Influence of inefficient changes suggested in A. A. Trani et al. (2024) and G. Fabj et al. (2026)	2×10^3	200
M13	The SG[1] model with $\dot{M}_{\rm out} = 0.1\dot{M}_{\rm Edd}$	Dependence on the disk model and the inflow rate	7×10^3	2000
M14	The SG model with $\dot{M}_{\rm out} = 0.01\dot{M}_{\rm Edd}$	”	4×10^3	180
M15	The TQM model with $\dot{M}_{\rm out} = 0.1\dot{M}_{\rm Edd}$	”	3×10^3	140
M16	The TQM model with $\dot{M}_{\rm out} = 0.01\dot{M}_{\rm Edd}$	”	7×10^2	57
M17	Super-Eddington accretion is allowed with $s = 0.5$	Influence of super-Eddington accretion	3×10^3	290
M18	Super-Eddington accretion is allowed with $s = 0.3$	”	3×10^3	460
M19	Consider transition to the zero-Bernoulli accretion (ZEBRA) state	Influence on the change in accretion prescription	3×10^3	840
M20	Consider transition to the ZEBRA state and $f_{\rm active} = 0.1$	”	3×10^3	200

Note. The input columns show the model number, and the differences with respect to the fiducial model, and the motivation for investigating each model. The output columns list the number of mergers at $t = 3$ Myr ($N_{\rm mer,10}$) and the top 1% of masses among merging binaries ($M_{\rm top1}$) among 10 simulations.
[1] E. Sirko & J. Goodman (2003, hereafter SG)

gravitational radius of the BH, and

$$r_{\rm wind} = \min(r_{\rm circ}, r_{\rm trap}), \tag{3}$$

where $r_{\rm circ}$ is the circularization radius, at which the gas becomes circularized, and $r_{\rm trap} \approx (\dot{M}_{\rm BHL}/\dot{M}_{\rm Edd}(m_{\rm BH})\eta_{\rm rad})r_{\rm g}$ is the spherical photon trapping radius (e.g., S. Kato et al. 2008), within which photons are advected inward faster than they can diffuse outward, $m_{\rm BH}$ is the mass of the stellar-mass BH, and $\eta_{\rm rad}$ is the radiative efficiency. Following the numerical simulations by S. Sagynbayeva et al. (2025), we set

$$r_{\rm circ} = f_{\rm circ}\, r_{\rm Hill}, \tag{4}$$

where $r_{\rm Hill} = R_{\rm BH}(m_{\rm BH}/3M_{\rm SMBH})^{1/3}$ is the Hill radius, $R_{\rm BH}$ is the distance from the SMBH to the BH, and $f_{\rm circ}$ is a factor estimated as

$$f_{\rm circ} \sim \min\{1,\, 0.01(m_{\rm BH}/M_{\rm SMBH})^2(R_{\rm BH}/H_{\rm AGN})^6\}, \tag{5}$$

where $H_{\rm AGN}$ is the scale height of the AGN disk. We set $s = 0.5$ for model M16 and $s = 0.3$ for model M17, considering the uncertainties suggested by numerical simulations (e.g., H. Hu et al. 2022; D. Toyouchi et al. 2024; P. C. Fragile et al. 2025).

In models M19–M20, we adopt the prescription suggested by M. C. Begelman & M. Volonteri (2017), where the transition between accretion states occurs based on the relationship between $r_{\rm circ}$ and $r_{\rm trap}$. This prescription is motivated by observations of accreting systems, such as tidal disruption events (E. R. Coughlin & M. C. Begelman 2014) and ultraluminous X-ray sources (J. Poutanen et al. 2007), and is consistent with 3D general relativistic radiation magnetohydrodynamic simulations (A. Sadowski & R. Narayan 2016; P. C. Fragile et al. 2025). When $r_{\rm circ}$ exceeds $r_{\rm trap}$, outflows reduce the accretion rate near the Eddington limit (Equation (2)), as predicted by the ADIOS model (R. D. Blandford & M. C. Begelman 1999). Conversely, if $r_{\rm circ}$ is smaller than $r_{\rm trap}$, shocked gas couples strongly to radiation due to efficient advection relative to diffusion, resulting in less efficient mass loss. This state is referred to as a ZEBRA flow (E. R. Coughlin & M. C. Begelman 2014). This process facilitates weak mass loss while allowing for super-Eddington accretion. Reflecting this suggestion, we assume that the accretion rate onto a BH is given by Equation (2) with $s = 1$ when $r_{\rm circ} > r_{\rm trap}$, and by the gas-capture rate $\dot{M}_{\rm BHL}$ when $r_{\rm circ} < r_{\rm trap}$. These slopes are supported by the numerical simulations (A. Sadowski & R. Narayan 2016; P. C. Fragile et al. 2025). Note that this prescription is also motivated by the possibility of producing strong electromagnetic counterparts to GW events, as suggested in V. Connaughton et al. (2016), Z. Bagoly et al. (2016), M. J. Graham et al. (2020, 2023), and S.-R. Zhang et al. (2026), without causing the overgrowth problem (H. Tagawa et al. 2026a). This problem arises when BHs grow too rapidly by continuously accreting most of the captured gas, which likely conflicts with Soltan's argument (Q. Yu & S. Tremaine 2002) and the dynamics of S stars (Gravity Collaboration et al 2020; H. Tagawa et al. 2022). In model M20, we reduce the accretion rate by a factor of 10 in both cases, considering a duty cycle of $\sim$0.1, as roughly estimated in H. Tagawa et al. (2022). Note that we do not model the transition to the ZEBRA state associated with kicks, despite that it is predicted, because its influence on the final mass is estimated to be minor (H. Tagawa et al. 2026a).

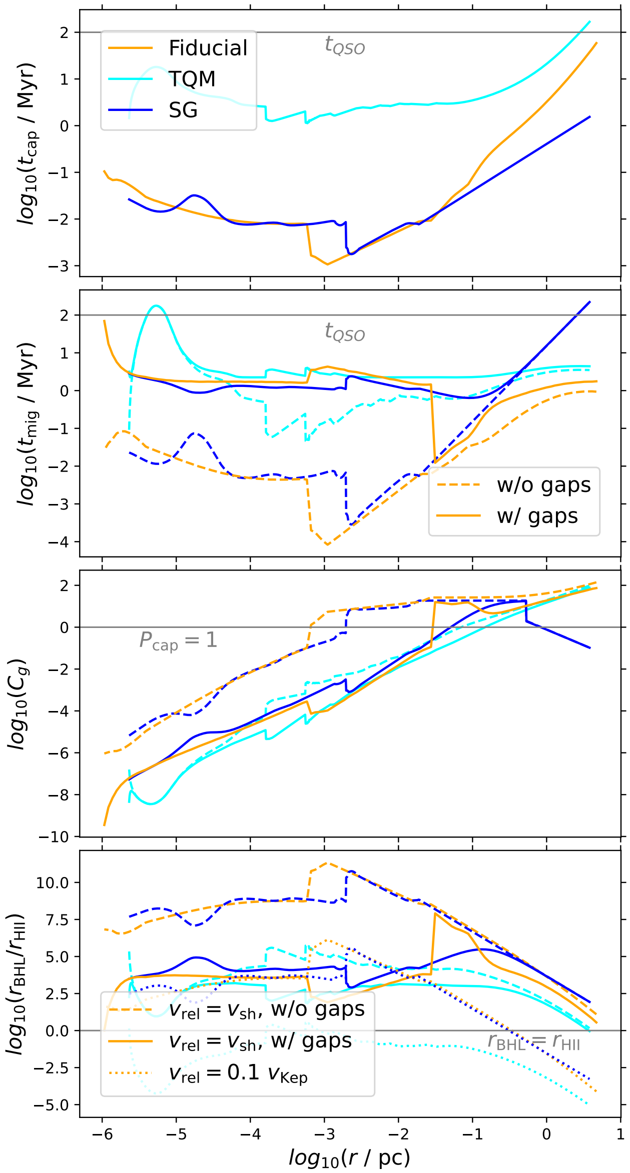

Figure 1. The timescales and conditions characterizing the evolution of 30 $M_\odot$ BHs in AGN disks. The orange, cyan, and blue lines represent the fiducial, TQM, and SG models, respectively. In the second to fourth panels, dashed and solid lines indicate results without and with gaps, respectively. The top panel shows the capture timescale for a BH with a relative velocity equal to 0.1 times the local Keplerian velocity with respect to the local AGN gas. The second panel shows radial migration timescales. The gray lines in the first and second panels denote the typical upper limit for the lifetime of AGNs per galaxy, approximately 100 Myr (P. Martini 2004). The third panel shows the probability that two encountered bodies form a binary via gas capture. The gray line indicates $P_{\rm cap} = 1$, above which binaries always form after an encounter. The fourth shows the ratio of the Bondi–Hoyle–Lyttleton radius to the size of an H II region. When this ratio exceeds unity, gas dynamical friction can operate for capture to the AGN disk, binary formation, and binary hardening, without being suppressed by radiative feedback. For the solid and dashed lines, the relative velocity between a BH and the gas is given by the shear velocity considering gas-capture binary formation, while for the dashed lines, it is given by 0.1 times the local Keplerian velocity considering capture by the AGN disk. The gray line represents $r_{\rm BHL} = r_{\rm HII}$, above which radiation feedback is inefficient.

To calculate the evolution of the BH spin direction, we estimate the warp radius (Equation (6) in H. Tagawa et al. 2020b), which is the radius at which the circum-BH disk aligns with the BH spin. For this calculation, we use the inflow rate at the warp radius in models M17–M20, unlike the fiducial model, which assumes the Eddington accretion rate regardless of radius. To account for the torque exerted by the circumbinary disk, we enhance its magnitude to reflect the actual accretion rate onto the BH.

2.4. Disk Prescriptions in Previous Studies

We briefly discuss previous studies that present suggestions different from our setup. Some studies claim that gap formation is inefficient (e.g., Z. Pan & H. Yang 2021a), while updated prescriptions (P. C. Duffell et al. 2014; K. D. Kanagawa et al. 2015, 2018) tend to favor gap formation (e.g., S. Gilbaum et al. 2025). In the presence of gaps, binary–single interactions have been found to be efficient (H. Tagawa et al. 2020c), influencing observable outcomes.

Y. Tomar et al. (2026) estimated that gaseous processes may become inefficient if magnetic fields are strong, as inferred by P. F. Hopkins et al. (2024). However, in this model, the inflow rate onto the SMBH is quite high, at approximately 0.1–1 times the star formation rate in the host galaxy, which may be inconsistent with the SMBH and galaxy (bulge) mass relation or typical Eddington rates of AGNs.

P. F. Hopkins et al. (2026) pointed out that the gas mass around SMBHs is constrained by the rotation speed of the gas, which disfavors the model that AGN disks with an α viscosity of $\alpha \lesssim 1$ extend to parsec scales, as proposed by SG. More efficient angular momentum transfer is required in the outer regions, as modeled by TQM and M. Epstein-Martin et al. (2025b). This motivates our use of TQM in the fiducial model M1.

3. Results

3.1. Bulk of Mergers

We present the distributions of observables in the fiducial model, and their dependence on various parameters. To demonstrate the distributions in this section, we performed 10 simulations with different realizations of random numbers characterizing the initial BH distributions, unless otherwise specified.

The evolution of BHs can be broadly understood from Figure 1, which summarizes the timescales and conditions relevant to gaseous processes. In the early phase, BHs with low velocities relative to the local AGN gas are gradually captured by the disk from the inner regions; the capture timescale is shown in the upper panel of Figure 1 (computed from Equation (26) of H. Tagawa et al. 2020c).[8] Once captured, BHs migrate within the AGN disk on the timescale shown in the second panel of Figure 1 (computed from Equations (17) and (18) of H. Tagawa et al. 2020c). During migration, BHs may form binaries upon encountering other BHs; the probability of binary formation is higher in the outer regions, as shown in the third panel of Figure 1. This probability is computed as the ratio of the azimuthal passing timescale to the damping timescale of the relative velocity due to gas dynamical friction (Equation (64) of H. Tagawa et al. 2020c), a criterion supported by recent numerical simulations (e.g., M. Dodici & S. Tremaine 2024). Gaseous processes—capture by the AGN disk, binary formation, and hardening—

[8] The capture timescale may be overestimated, particularly in the inner regions of $r \lesssim 10^{-2}$ pc, where the Hill mass becomes smaller than $\sim$0.1 times the BH mass (C. Rowan et al. 2025b; H. Whitehead et al. 2025).

are effective only when the Bondi–Hoyle–Lyttleton radius ($r_{\rm BHL}$) exceeds the size of the H II region (the possible influence of X-ray photons is ignored; M. Epstein-Martin et al. 2025b); this ratio is shown in the fourth panel of Figure 1 (e.g., Section 3.3.3 of H. Tagawa et al. 2020c). We calculate $r_{\rm BHL} = Gm_{\rm BH}/(v_{\rm rel}^2 + c_{\rm s}^2)$, where G is the gravitational constant, $v_{\rm rel}$ is the relative velocity between a BH and the local gas, and $c_{\rm s}$ is the sound speed of the local AGN gas. For gas-capture binary formation, $v_{\rm rel}$ is approximately equal to the shear velocity, while in binary hardening, it is determined by the rotation velocity of the binary. Gas-capture binary formation is typically unaffected by radiative feedback (solid lines in the bottom panel of Figure 1), whereas gas dynamical friction on hard binaries with a rotation velocity significantly higher than the shear velocity can be less effective as $r_{\rm BHL} \propto v_{\rm rel}^{-2}$. In the outer regions, radiation feedback often prevents the capture of BHs into the AGN disk, particularly when the relative velocity is high. It is noteworthy that the reduction of gas density due to gap formation facilitates mergers driven by binary–single interactions, while mergers are primarily driven by gaseous torques when gap formation is turned off in the fiducial model, according to our test calculation. Examples of the time evolution of binary parameters can be found in previous studies (H. Tagawa et al. 2020b, 2020c), which are similar in the updated models adopted here. We present histograms of the BH population to quantify their evolution and merger properties next.

3.1.1. Merging Black Hole Masses and Mass Ratio

Figure 2 shows the chirp and primary BH mass distributions of the mergers in models M1–M20 on a linear scale; Figure 3 shows the total mass and mass ratio distributions on logarithmic and linear scales, respectively; and Figure 4 shows the 2D distribution as a function of the primary and secondary BH mass in the merging binaries.

The results for the fiducial model (model M1) at $t = 1$, 3, 10, and 30 Myr are displayed in the leftmost panels. For the other models, results at $t = 3$ Myr are shown unless the duration is explicitly stated. These 1D histograms are linearly interpolated to enhance visualization, when error regions are not included.

In the fiducial model, accretion is capped at the Eddington rate, and the initial BH mass is below $30\,M_\odot$. In the early phases, much shorter than the Salpeter timescale of ∼40 Myr, massive BHs of $\gtrsim 40\,M_\odot$ grow primarily through mergers. As time passes, the frequency of massive mergers increases (see the leftmost panels in Figures 2–3), mainly due to hierarchical mergers. For example, more than 90% of the mass of merging BHs with $m_{\rm BH} > 100\,M_\odot$ is attributed to hierarchical mergers for $t \leqslant 10$ Myr, while the remaining mass ($\lesssim$10% of the total merging masses) comes from accretion. For $t \gtrsim 10$ Myr (red and cyan lines), the model overproduces high-mass mergers ($M_{\rm chirp} \gtrsim 70\,M_\odot$) relative to the intrinsic merging-mass distribution as estimated by LVK observations after accounting for detection efficiency (dashed and dotted lines). Hence, in the fiducial model, the predicted mass distribution agrees with the observed distribution only for $t \lesssim 3$ Myr.

The second panels in Figures 2–3 show the merging-mass distributions for models M2–M5. These models explore variations in the the number of BHs within an AGN disk by altering the initial velocity distribution of BHs, which affects the timescale for capture by the disk (orange, blue, and red lines), or by changing the total number of BHs (cyan lines). As the number of BHs decreases, the rate of mergers among massive BHs also declines. This decrease can be offset by extending the duration t (blue line). Therefore, although the effects of the number of BHs in an AGN disk and the duration of AGN phases on the merging-mass distribution are degenerate, their combination can be constrained by comparing with the observed mass distributions.

The third panels of Figures 2–3 depict variations in the geometry of binary–single interactions (orange lines), the SMBH mass (blue lines), the gas inflow rate toward the SMBH (red lines), and the initial BH masses (cyan lines). These parameters influence the merging-mass distribution. In model M5, the 1D binary–single interactions efficiently drive mergers with fewer binary–single interactions. In model M6 where the SMBH mass is high, the capture time to the AGN disk is extended due to the large Keplerian velocity, reducing the total number of mergers. However, a prolonged migration time in the inner region increases the fraction of hierarchical mergers. Model M7 shows that a higher gas density results in efficient BH capture by the AGN disk, thus increasing the number of mergers. In model M8, higher initial masses for first-generation BHs generally lead to higher merging masses, enhanced by a certain factor. By comparing the predictions with the observed mass distribution, we can potentially constrain these parameters.

The fourth panels show the impact of varying prescriptions for the capture, migration, and binary–single interactions. In the absence of migration (orange lines), BHs are inhibited from accumulating, which somewhat suppresses mergers among higher-generation BHs. However, the effects of changes in migration (as in models M9 and M10, orange and blue lines, respectively) on the mass distribution are not drastic, since migration typically takes $\gtrsim$megayear for many BHs in the fiducial setting, partly due to the low $\dot{M}_{\rm out}$. The influence of the radiation feedback (red lines) on merging masses is also not significant, as mergers can still occur through binary–single interactions even when gas hardening by dynamical friction becomes inefficient. In the model with no change in orbital angular momentum during binary–single interactions (cyan lines), mergers among high-mass BHs become moderately more frequent. This is because binaries tend to merge with their orbital angular momentum (anti-) aligned with BH spins, which reduces the recoil kick velocity during mergers among higher-generation BHs, thereby increasing the frequency of these mergers.

In the fifth panels, the dependence on disk models is examined. The frequency of highly massive mergers is higher in the SG model (orange and blue lines) and lower in the TQM models (red and cyan lines). In the SG model, mergers involving massive BHs are more frequent, because the higher gas surface density in the outer regions, resulting from less efficient angular momentum transfer, facilitates BH capture into the AGN disk and binary formation (the upper panel of Figure 1). In contrast, the TQM model exhibits the opposite trend. Similarly, higher inflow rates lead to more frequent massive BH mergers (orange and red lines in the fifth panels of Figures 2–3), as also seen in model M7. Note that in the fiducial model, the angular momentum transfer efficiency is comparable to that in the TQM and SG models in the outer and inner regions, respectively, reflecting the transition from global

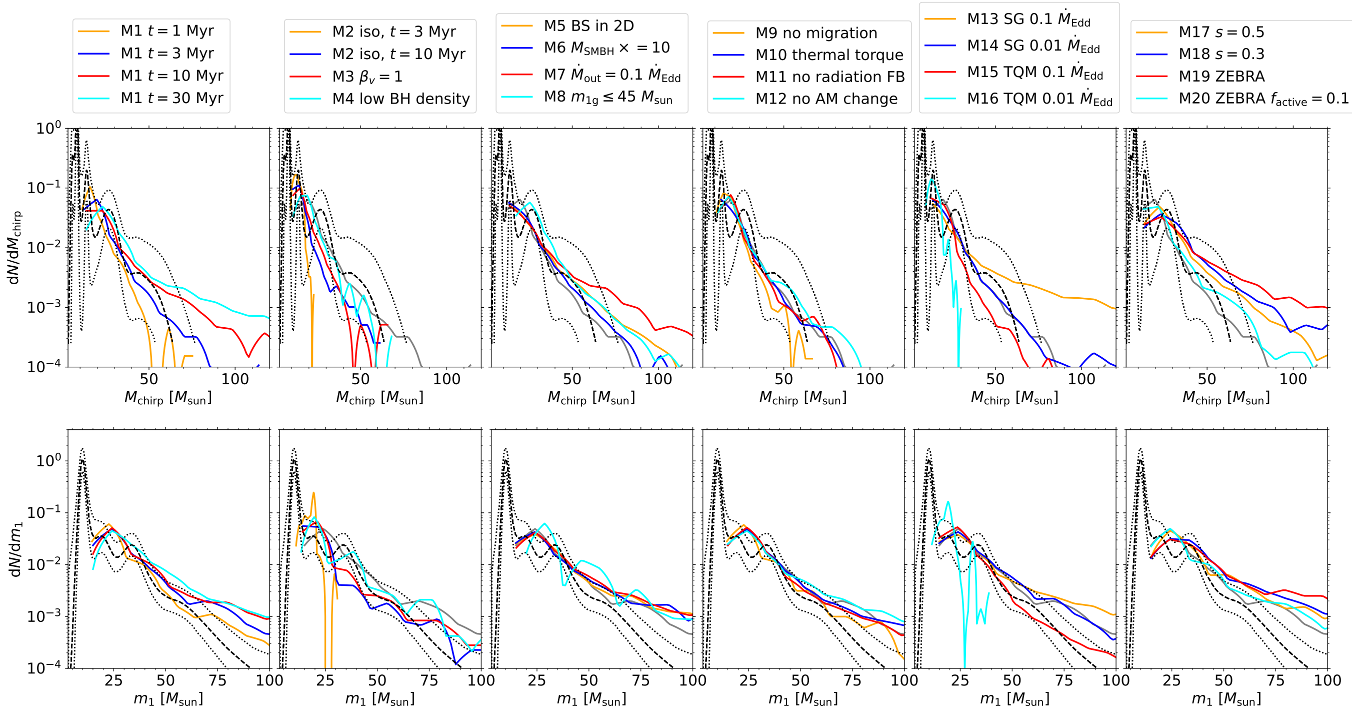

Figure 2. The linearly interpolated distribution of chirp mass (top row) and the primary BH mass (bottom row) of the merging binaries for models M1–M20. For model M1 (leftmost panel), the results at $t = 1$–30 Myr are presented, while those at $t = 3$ Myr are shown for the other models (other panels). The dashed and dotted black lines represent the median and the 90% credible intervals inferred from the LVK the first observing run (O1)– the third observing run (O3) data (V. Tiwari 2024). The gray lines show the results for model M1 at $t = 3$ Myr for reference. The dashed and dotted black lines in the bottom row of panels represent, respectively, the median and the 90% credible intervals for LVK O1– the first part of the fourth observing run (O4a) data estimated using B-spline model in The LIGO Scientific Collaboration et al. (2026b).

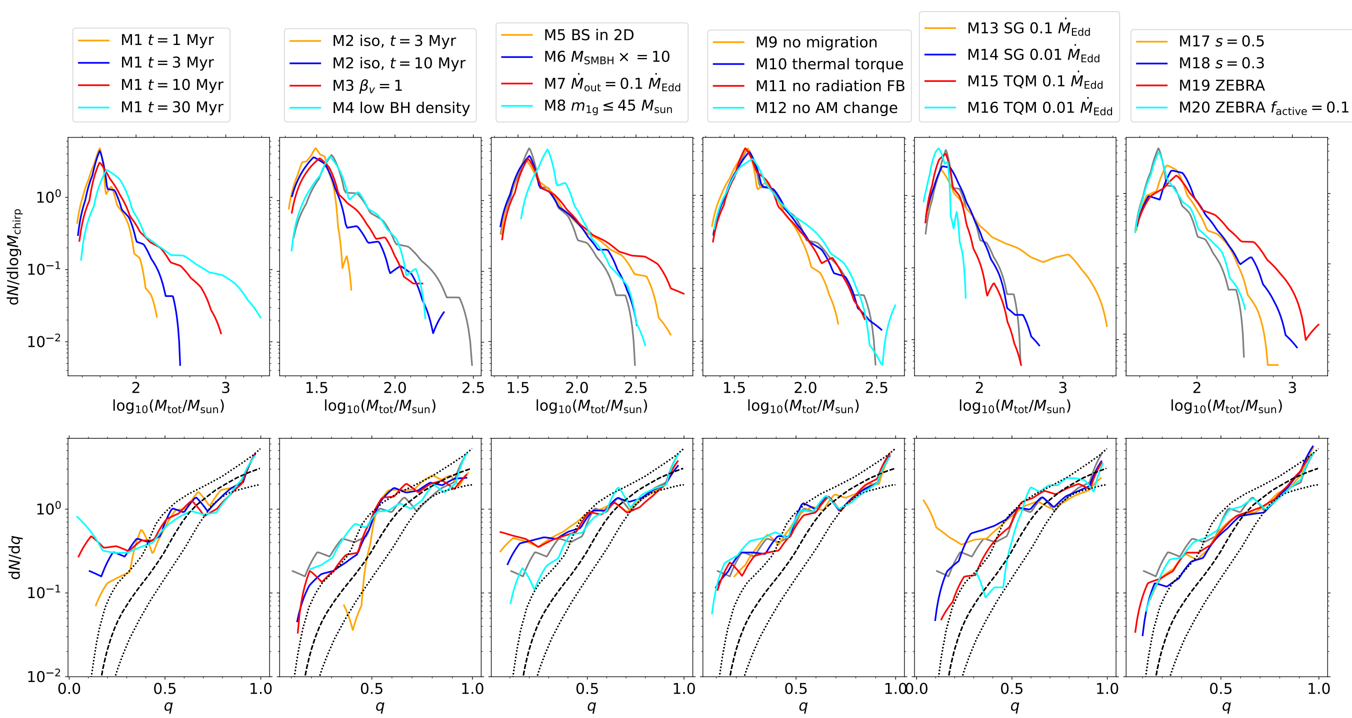

Figure 3. Similar to Figure 2, but showing the binary mass ($M_{\rm tot}$ top row) and mass ratio (bottom row) distribution on logarithmic and linear scales, respectively. Dashed and dotted black lines represent, respectively, the median and the 90% credible intervals for LVK O1–O4a data estimated using the broken power law + peak model in The LIGO Scientific Collaboration et al. (2026b).

to local torques. Thus, the disk model significantly impacts the merging-mass distribution, primarily due to differences in gas density.

The sixth panels explore variations in accretion prescriptions. For the models with $s \leqslant 0.5$ (orange and blue lines), and those considering the transition to the ZEBRA state (red lines),

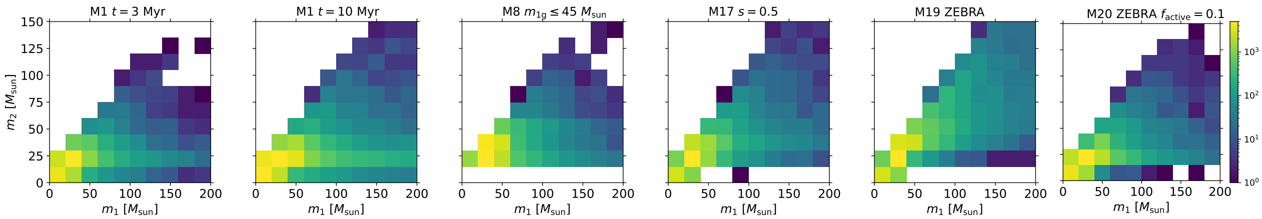

Figure 4. The distribution of primary and secondary BH masses in mergers. To reduce Poisson noise, we performed 100 simulations.

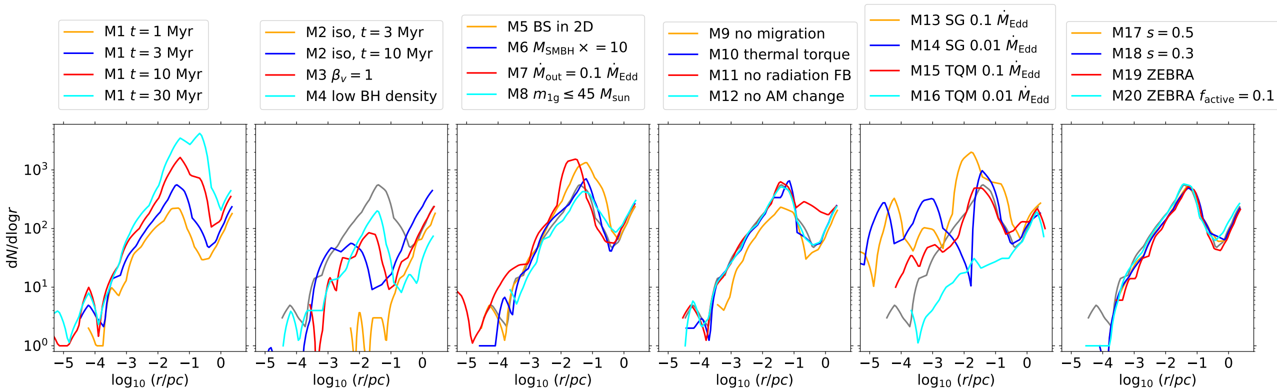

Figure 5. The linearly interpolated distribution of the distance from the SMBH of the mergers for models M1–M20.

the rate of massive BH mergers significantly exceeds observations. Therefore, if this channel contributes to a portion of the observed events, the efficiency of BH growth via accretion should be moderate. On the other hand, when the duty cycle of accretion is reduced to 0.1 (cyan lines), as roughly estimated by H. Tagawa et al. (2022), the merging-mass distribution aligns more closely with observations, even when accounting for the transition to the ZEBRA state.

The bottom panels in Figure 3 show the mass ratio distributions, along with their observed distribution, which is also model dependent (see S. Colloms et al. 2025; The LIGO Scientific Collaboration et al. 2026b). Models with chirp mass distributions that are inconsistent with observations (specifically, model M1 at $t \gtrsim 10$ Myr and models M5, M6, M7, and M13 at $t = 3$ Myr) also show similar discrepancies in the mass ratio distribution. This occurs because frequent hierarchical mergers tend to produce massive remnants that pair with lower-mass objects, resulting in low-mass ratio mergers. Such very low-q mergers are less frequent in cluster models due to the lower escape velocity of the system (e.g., C. L. Rodriguez et al. 2016), preventing the formation of massive BHs through hierarchical mergers. An exception to this trend is observed in the highly accreting models (M17–M20), where the BH masses grow substantially due to gas accretion. This increases both the component masses and the mass ratios, producing frequent high-mass-ratio mergers that are broadly consistent with the observed distribution.

Overall, the merging-mass and mass ratio distributions are influenced by several parameters, particularly the duration of the AGN phase, the AGN gas density, the BH number density within the AGN disk, and the accretion prescriptions. If a substantial fraction of mergers originates from AGN disks, observational data can be used to constrain the combination of these parameters.

Although we do not alter several parameters, the key parameters affecting the merger rate and the maximum BH masses found in L. Xue et al. (2025) are related to the BH number and AGN disk densities, as explored in this study. Table 2 lists the number of mergers and the top 1% of masses among merging binaries. The dependence on these parameters is mostly consistent with the results from L. Xue et al. (2025), while the maximum mass is higher by a factor of a few in this study. This discrepancy is presumably due to the implementation of binary component exchanges and the evolution of background BHs through mergers and accretion, which tends to produce more massive binaries and merger remnants. Specifically, the absence of exchanges during binary–single interactions and the growth of background objects through mergers can, respectively, reduce the mass enhancement at mergers by up to a factor of ∼3 (reflecting the initial BH mass range) and by a factor of the expected number of generations of merging background BHs.

In the fiducial model, the AGN lifetime needs to be less than ∼3 Myr, limited primarily by BH number density. Currently, the fiducial model aligns with the observed constraints. If the accretion rate onto BHs is characterized by a super-Eddington rate, the duty cycle of the accretion phase should be low as investigated in model M20, or substantial wind losses may regulate accretion (e.g., A. Sadowski & R. Narayan 2016). These variations among models could be further constrained through comparisons with other observables.

3.1.2. Merger Location

Figures 5 and 6 shows the distribution of radial distances of the mergers (r) from the SMBH, and Figure 7 presents the distributions for both the r and the binary mass at merger. Specifically, Figure 5 shows the overall distribution, while Figure 6 presents the distribution for different binary formation mechanisms. Figures 6 and 7 depict results across models M1, M4, M5, M13, and M15, selected because they exhibit variations in merger locations. In both the fiducial and many other models, two peaks appear near ∼0.01–0.05 and ∼3 pc.

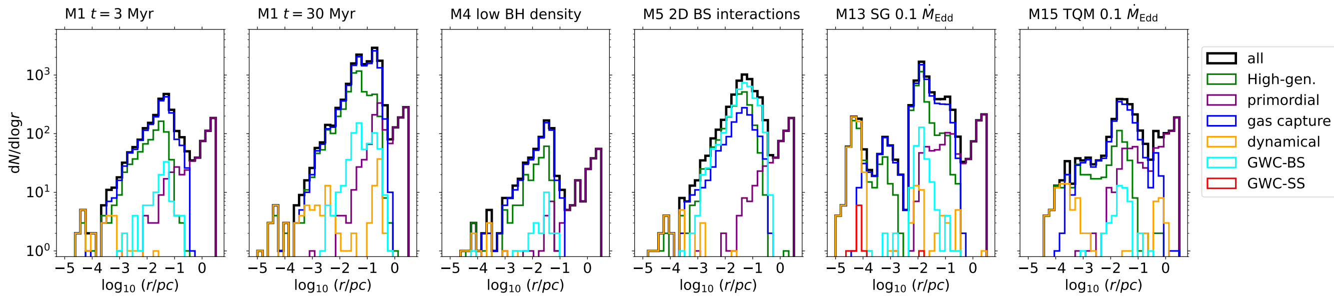

Figure 6. The distribution of the distance of mergers from the SMBH for different binary formation mechanisms in models M1, M4, M5, M13, and M15. The purple, blue, orange, red, and cyan lines represent mergers from binaries formed as primordial binaries, through gas-capture processes, dynamical interactions, GWC during single–single interactions, and GWC mechanisms during binary–single interactions, respectively. We also present the merger locations for binaries containing higher-generation BHs by the green line.

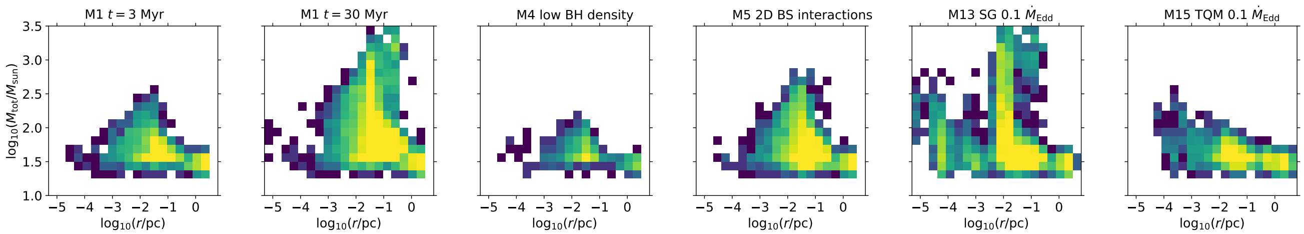

Figure 7. The distribution of the binary mass and their distance from the SMBH for all merging BHs in models M1, M4, M5, M13, and M15.

The outer peak is dominated by primordial binaries (purple lines in Figure 6). These mergers occur slowly due to the low gas density, and are typically between a pair of first-generation BHs. Remnant BHs merged at $\sim$1 pc often escape by GW kicks, resulting from the shallower gravitational potential of an SMBH. They are inefficiently recaptured by AGN disks due to lower gas density, leading to infrequent hierarchical mergers (Figure 7).

Generally the mergers near the inner peak $\sim$0.01–0.05 pc are dominated by gas-assisted binary formation. In this region BHs are captured by the disk earlier due to the higher gas surface densities there and more frequent disk crossings (the top panel of Figure 1). After their capture, BHs migrate, form binaries due to gas, and merge rapidly, with most hierarchical mergers occurring in this region (Figure 7). Over time, the radial location of mergers involving higher-generation BHs gradually extends to the $\sim$parsec regions (green line in the second panel of Figure 6) as the BHs get captured in the disk in these regions as well.

In the inner regions, binary–single interactions take place, and merging binaries form through a GWC process during these interactions (cyan lines in Figure 6). Since the fraction of mergers resulting from this process ($\sim$5%–10%; H. Tagawa et al. 2021b) is comparable to that in cluster models (e.g., C. L. Rodriguez et al. 2018; M. Zevin et al. 2021), the frequency of binary–single interactions before mergers is likely to be similar. Note that this rate might be significantly enhanced by dense gas accumulated around a binary, as the ejection of this gas during interactions can significantly harden the three-body system (C. Rowan et al. 2025c; H. Tagawa et al. 2026b). Mergers via this process become highly frequent if binary–single interactions occur in a 2D plane, in that case dominating over the gas-assisted binary formation pathway (cyan lines in the fourth panel of Figure 6). Unlike in our previous papers (e.g H. Tagawa et al. 2021b), binary formation and mergers through single–single GWC encounters are rare in all of our models, due to the updated encounter probabilities described in Section 2.2.

In cases of low BH number density (models M2–M4), mergers are less frequent in the inner regions, as the chances of encounters with other BHs and the binary formation are reduced. Hence, mergers among massive BHs are infrequent in these models (e.g., Figure 7).

The location of mergers is significantly influenced by the choice of AGN disk model. In the SG model, mergers via the gas-capture process become inefficient around several $\times\, 10^{-3}$ pc (dip features in orange and blue lines in the fifth panel of Figure 5). This is due to enhanced opacity from dust sublimation, which increases the scale height and reduces the gap depth, thereby shortening the migration timescale (solid blue line in the second panel of Figure 1). Note that this change in opacity appears in the inner regions of $\lesssim 10^{-3}$ pc in the fiducial model, though its effects are not particularly prominent. Furthermore, binaries often merge through three-body encounters and GWC during single–single interactions at distances of several $\times\, 10^{-5}$ pc. This is attributed to the iron opacity bump (Y.-F. Jiang et al. 2016), which is implemented only in the SG model developed by D. Gangardt et al. (2024) among the disk models we used. In this region, the migration timescale increases especially for smaller BHs, leading to elevated merger rates. In the TQM model with $\dot{M}_{\rm SMBH} = 0.1\dot{M}_{\rm Edd}$, mergers are relatively frequent within 10^{-3} pc because the inward migration timescale increases there. This effect is less prominent in the TQM model with $\dot{M}_{\rm SMBH} = 0.01\dot{M}_{\rm Edd}$.

Merger locations may be directly constrained by the detection of Doppler acceleration for in-spiraling sources using future GW facilities (K. Inayoshi et al. 2017; Y. Meiron et al. 2017; K. W. K. Wong et al. 2019; K. Hendriks et al. 2024; S.-C. Yang et al. 2025; L. Zwick et al. 2025; H. Tagawa et al. 2026b; K. Hendriks et al. 2026) and/or using the detection or nondetection of a lensed secondary GW signal by the central SMBH (L. Gondán & B. Kocsis 2022). Combining with the expected properties of merging BH population

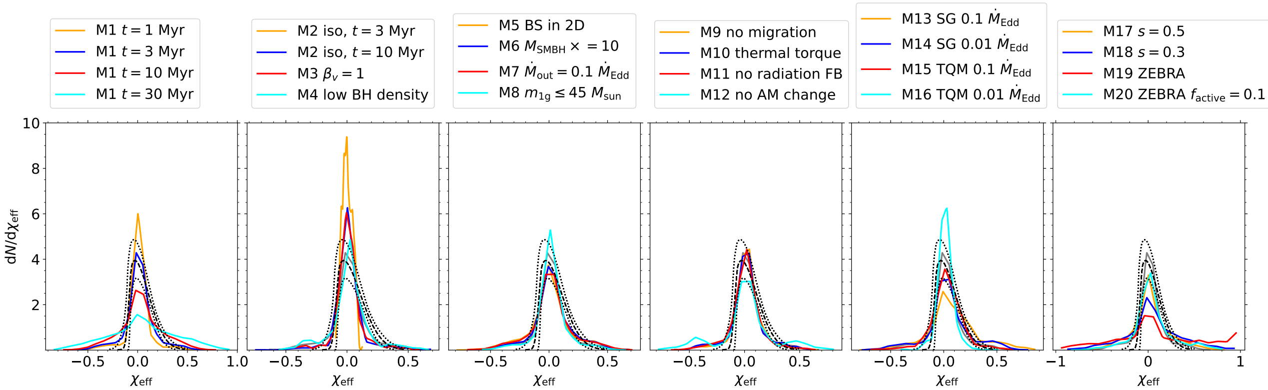

Figure 8. Similar to Figure 2, but the distribution of $\chi_{\rm eff}$ is shown. The dashed and dotted black lines represent, respectively, the median and the 90% credible intervals for LVK O1–O4a data estimated using the skew-normal effective spin model in The LIGO Scientific Collaboration et al. (2026b).

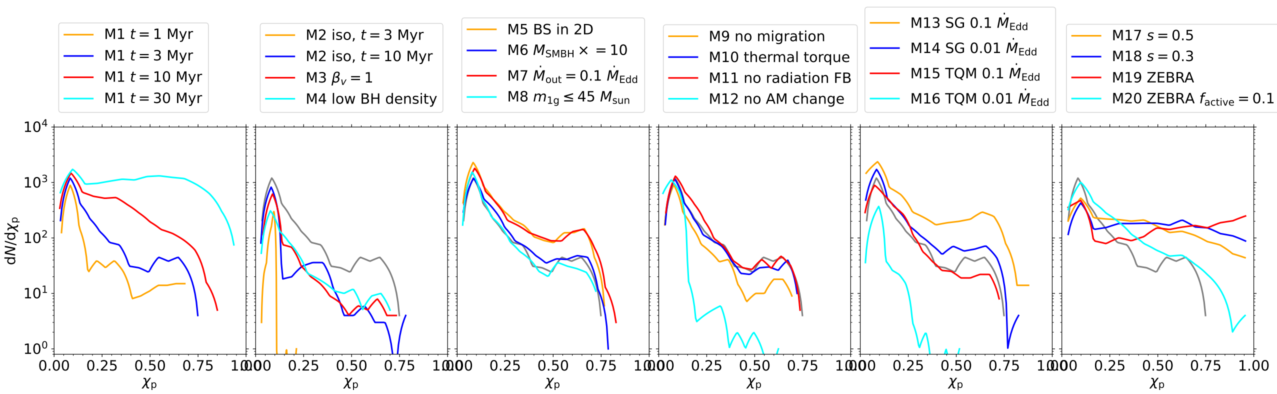

Figure 9. Similar to Figure 2, but the distribution of $\chi_{\rm p}$ is shown.

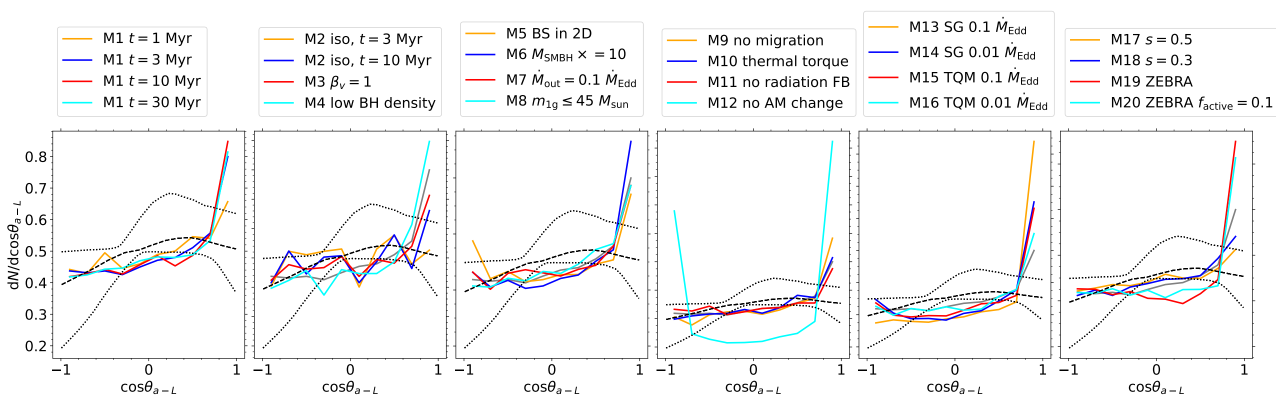

Figure 10. Similar to Figure 2, but the distribution of $\cos(\theta_{a-l})$ is shown. The dashed and dotted black lines represent, respectively, the median and the 90% credible intervals for LVK O1–O4a data estimated using the Gaussian component spins model.

discussed in this paper, this could offer novel indirect constraints on the properties of AGN disks.

3.1.3. Spin Tilts

The distributions of $\chi_{\rm eff}$ and $\chi_{\rm p}$ are constrained by observations, providing valuable information on the astrophysical models involving the mergers. Figures 8 and 9 show the $\chi_{\rm eff}$ and $\chi_{\rm p}$ distributions for models M1–M20. Figure 10 shows the distributions of the angle between the BH spin and the orbital angular momentum direction of merging binaries (θ_{a-l}), which is useful for understanding the $\chi_{\rm eff}$ and $\chi_{\rm p}$ distributions.

In the fiducial model, $\chi_{\rm eff}$ and $\chi_{\rm p}$ peak at zero, as most mergers involve first-generation BHs with spin magnitudes around ∼0.1. A subset of these mergers is contributed by higher-generation BHs, which typically have spin magnitudes around ∼0.7. The distribution of θ_{a-l} results from the interplay between alignment due to the Bardeen–Peterson effect and randomization by binary–single interactions, leading to a broad distribution around $\cos(\theta_{a-l}) = 1$. Consequently, the $\chi_{\rm eff}$ and $\chi_{\rm p}$ values for higher-generation mergers are spread over the ranges ∼−0.7 to ∼0.7 and 0 to ∼0.7, respectively, with a weak asymmetry in the $\chi_{\rm eff}$ distribution.

Over time, the fraction of mergers involving higher-generation BHs increases, which broadens the $\chi_{\rm eff}$ and $\chi_{\rm p}$ distributions. In contrast, if the proportion of hierarchical

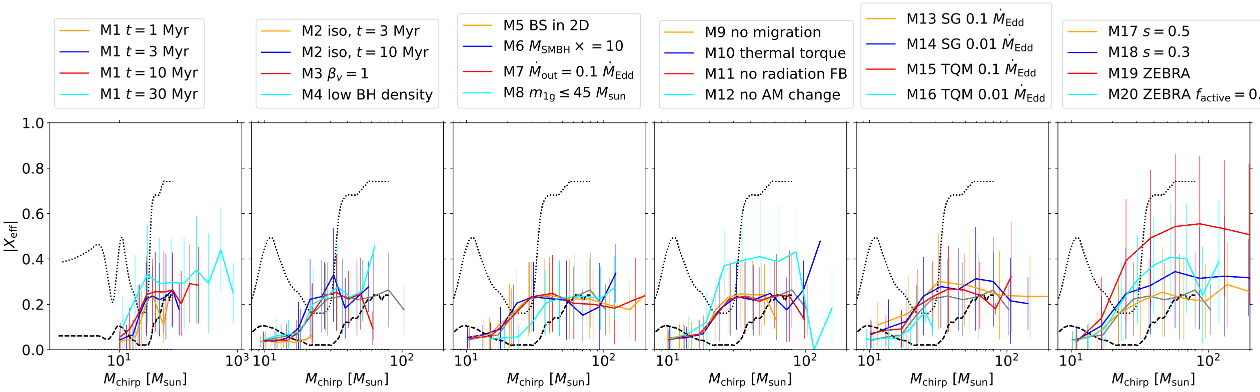

Figure 11. The average and dispersion of the absolute value of the effective spin parameter as a function of the chirp mass for models M1–M20. The dashed and dotted black lines represent, respectively, the median and the 90% credible intervals for the aligned spin magnitude χ_z, as inferred from the LVK O1–O4a data estimated in The LIGO Scientific Collaboration et al. (2026b). When the number of mergers in a bin is fewer than two, we do not present the dispersion.

mergers is low (e.g., models M2–M4 and M16), $\chi_{\rm eff}$ and $\chi_{\rm p}$ both become concentrated in a narrow range around zero.

In cases where the binary angular momentum direction is not randomized during binary–single interactions (model M12), the angular momentum directions of binaries are typically aligned or antialigned with respect to the angular momentum direction of the AGN disk. For first-generation BHs, BH spins evolve through gas accretion, leading to a reduced θ_{a-l}. For higher-generation BHs, the spin magnitude is significantly increased through mergers, causing their spin directions to align with the angular momentum direction of the merged binary. The angular momentum direction of binaries formed through gas capture (as well as GWC during single–single interactions) is set to be either prograde or retrograde with respect to the AGN disk rotation, with equal probabilities. Consequently, the BH spin directions for high-generation BHs are typically (anti-)aligned with the binary angular momentum direction (two peaks in the fourth panel of Figure 10). This alignment results in a broader distribution of $\chi_{\rm eff}$ and a narrower distribution of $\chi_{\rm p}$, compared to other models.

When accretion is highly efficient, BH spin directions quickly align with the binary angular momentum directions via the Bardeen–Petterson effect (red and cyan lines in the sixth panel of Figure 10), while their spin magnitudes significantly increase in the model with efficient gas accretion (model M19, e.g., the sixth panel of Figure 19). In model M19, these effects produce a broad, asymmetric distribution of $\chi_{\rm eff}$ relative to zero, with higher values of $\chi_{\rm p}$. Furthermore, in the SG model with high accretion rates (model M13), the alignment process operates efficiently due to the high gas density, particularly in the outer regions, leading to a reduction in θ_{a-l}.

Observations constrain the distribution of θ_{a-l}, suggesting it is broad. The LIGO Scientific Collaboration et al. (2026b) estimated a possible peak in $\cos(\theta_{a-l})$ near zero (see also A. M. Farah et al. 2026; Y.-J. Li et al. 2026), although a peak near one cannot be ruled out; S. Vitale et al. (2025) noted that a peak near one tends to be underestimated. Consequently, the fiducial and many other models are not ruled out by the observed distribution, while model M12, which prefers $\cos(\theta_{a-l}) \sim -1$, is likely disfavored.

Although the observed $\chi_{\rm p}$ distribution is reported by The LIGO Scientific Collaboration et al. (2026b), it may contain a significant bias. This speculation arises because $\chi_{\rm p}$ should be lower than the spin magnitude of merging BHs, while the peak of the $\chi_{\rm p}$ distribution exceeds the peak of the spin magnitude distribution. Therefore, we refrain from directly comparing our results to the observed distribution.

For the distribution of $\chi_{\rm eff}$, the peak values appear to be consistent with the observed data; however, negative $\chi_{\rm eff}$ values are overproduced in some of the models. The fraction of mergers with $-0.3 \lesssim \chi_{\rm eff} \lesssim -0.2$ is model dependent, while those with $\chi_{\rm eff} \lesssim -0.4$ are likely rare. Only a few events may exhibit such values, such as GW241110, which has $\chi_{\rm eff} = -0.28^{+0.23}_{-0.20}$ (A. G. Abac et al. 2025b). We find that the fraction of mergers with $\chi_{\rm eff} < -0.4$ is $\sim$1% in the fiducial model, which is roughly consistent with the observed $\chi_{\rm eff}$ distribution. However, it is higher, around $\sim$4%, in models M12, M13, and M14. In models M18, M1 at $t = 30$ Myr, and M19, the fractions are 8%, 10%, and 15%, respectively. As a result, the contribution from these models to the observed events can be constrained to be minor. Nevertheless, caution may be needed in comparison, as the observed $\chi_{\rm eff}$ distribution could also be somewhat biased (e.g., A. R. Williamson et al. 2017).

3.1.4. Spin and Mass

Here, we present the correlation between mass and spin, as well as between mass ratio and spin, as suggested by observed GW data (T. A. Callister et al. 2021; H. Tagawa et al. 2021a; C. Adamcewicz & E. Thrane 2022; C. Adamcewicz et al. 2023; Y.-J. Li et al. 2024, 2026b; G. Pierra et al. 2024; F. Antonini et al. 2025; The LIGO Scientific Collaboration et al. 2026a, 2026b; H. Tong et al. 2025; A. M. Farah et al. 2026; C. Plunkett et al. 2026; A. Vijaykumar et al. 2026; Y.-Z. Wang et al. 2026a).

Figure 11 shows the average and dispersion of the absolute value of $\chi_{\rm eff}$ as a function of $M_{\rm chirp}$. In the higher $M_{\rm chirp}$ bins, the number of mergers is often small, making the estimates of the average and dispersion less robust. We observe an increase in $|\chi_{\rm eff}|$ at low masses, followed by a plateau at higher masses in most models. This plateau arises from hierarchical mergers, as the spin magnitudes of remnant BHs tend to cluster around $\sim$0.7. The minimum mass of the plateau roughly corresponds to the maximum initial mass of first-generation BHs (H. Tagawa et al. 2021a); this boundary shifts in model M8, where the maximum initial BH mass is changed.

Above this mass, several models show larger mean $|\chi_{\rm eff}|$ ($|\chi_{\rm eff}| \gtrsim 0.3$) than the fiducial model ($|\chi_{\rm eff}| \sim 0.2$) at $t = 3$ Myr. This behavior appears in highly accreting models

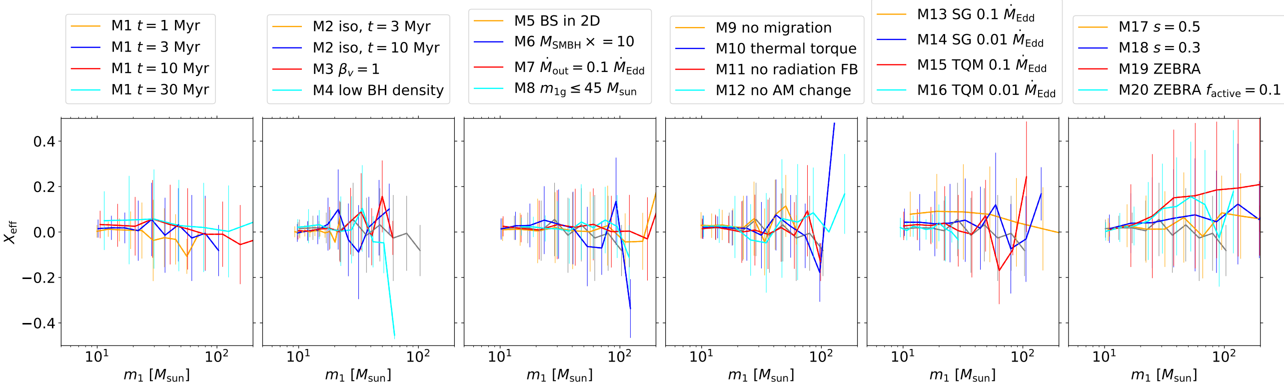

Figure 12. The average and dispersion of $\chi_{\rm eff}$ as a function of m_1 for models M1–M20.

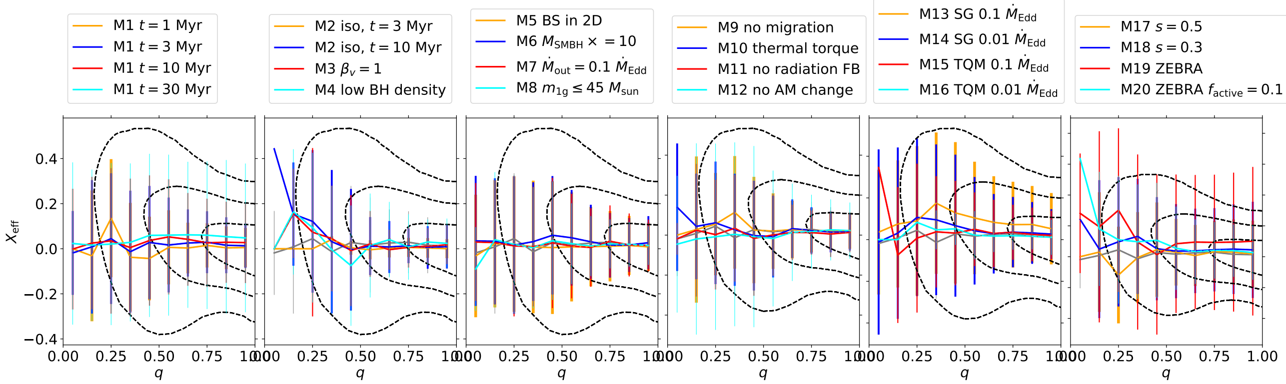

Figure 13. The average and dispersion of the effective spin parameter as a function of the mass ratio for models M1–M20. The three black lines represent 50%, 90%, and 99% credible regions inferred from the LVK O1–O4a data estimated using the linear model in The LIGO Scientific Collaboration et al. (2026b).

(models M17–M19), SG models (models M13 and M14), the model with no change in orbital angular momentum during binary–single interactions (model M12), and in the fiducial model at $t = 30$ Myr. These differences reflect BH spin evolution due to accretion and smaller angles between BH spins and the binary orbital angular momentum (e.g., in model M12). Thus, the plateau contains information useful for constraining accretion processes and interactions among BHs.

An increase and plateau in the $M_{\rm chirp}$–spin plane has been implied from GW data (H. Tagawa et al. 2021a; Y.-J. Li et al. 2024; G. Pierra et al. 2024; F. Antonini et al. 2025; Y.-Z. Wang et al. 2026a), which can help constrain model parameters. Dashed and dotted lines represent, respectively, the median and 90% credible interval for aligned spin magnitude from The LIGO Scientific Collaboration et al. (2026b). Although current constraints are weak, they indicate a possible increase in $|\chi_{\rm eff}|$ at high masses, along with a slight increase around $\sim 10\,M_\odot$, likely contributed by hierarchical mergers within a subpopulation (H. Tong et al. 2025; A. M. Farah et al. 2026; C. Plunkett et al. 2026). Potential locations for these events include dense star clusters with high metallicity (C. S. Ye et al. 2026). Additionally, this subpopulation may consist of in situ formed stars with higher metallicity, while more massive components could originate from the migration of globular clusters with lower metallicity in AGN environments (K. Fahrion et al. 2021, 2022). Comparing models to these intervals, except for the possible increase in low-mass regions, most models slightly exceed the 90% credible region around $\sim 30\,M_\odot$, while the model with more massive first-generation BHs (model M8) aligns better with the median. The observed median also suggests higher maximum first-generation BH masses above $\sim 45\,M_\odot$. With tighter observational constraints, the formation and evolution of first-generation BHs will be more tightly constrained. Hence, the correlation between mass and spins provides valuable insight into the properties of first-generation BHs, accretion mechanisms, and interactions between BHs.

Y.-J. Li et al. (2026b) demonstrate a correlation between θ_{a-l} (or $\chi_{\rm eff}$) and the mass of merging BHs. Notably, an increase in θ_{a-l} (or $\chi_{\rm eff}$) is observed in mergers within the upper-mass gap regions, posing challenges to various models. They found that mergers with high spin magnitudes tend to populate around $\chi_{\rm eff} \sim 0.2$–0.5 (or $\cos(\theta_{a-l}) \gtrsim 0.5$) and $m_1 \gtrsim 40\,M_\odot$ (we do not show this in the figure).

To explore this correlation, Figure 12 shows the relationship between $\chi_{\rm eff}$ and m_1. For most models, no significant correlation is observed. However, models with high accretion rates show a correlation. This is because accretion torques the binary angular momentum toward the prograde direction of the AGN disk, resulting in merged remnants having a similar spin direction. When these remnants merge again, they tend to exhibit small θ_{a-l} or high $\chi_{\rm eff}$, reproducing the observed correlation. The mass range and typical magnitude of $\chi_{\rm eff}$ for the high $\chi_{\rm eff}$ events are roughly consistent with the findings of Y.-J. Li et al. (2026b), offering a plausible model that explains these observations.

Figure 13 shows the correlation between the mass ratio (q) and $\chi_{\rm eff}$. Contrary to the observational implications presented by T. A. Callister et al. (2021), C. Adamcewicz & E. Thrane (2022), C. Adamcewicz et al. (2023), and Y.-J. Li et al. (2025),

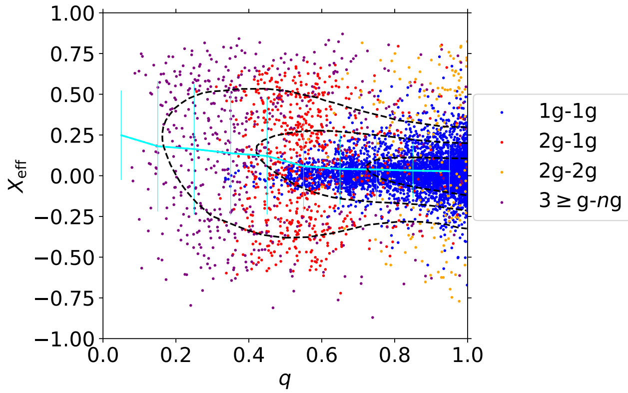

Figure 14. Same as Figure 13, but for model M20, with the distribution of mergers shown. The median and dispersion of $\chi_{\rm eff}$ are calculated by performing 100 simulations, to reduce a bias caused by Poisson noise. Mergers among first generation–first generation, second generation–first generation, second generation–second generation, and third-generation and higher BHs are represented by blue, red, orange, and purple points, respectively, for 20 simulations (for visualization purposes).

most of our models do not show a clear correlation between q and the average of $\chi_{\rm eff}$. This is because binary orbital angular momentum directions are randomized by binary–single interactions, and mergers usually occur before BH spins align with the binary orbital angular momentum via gas accretion. Note that in the model that does not randomize angular momentum directions during binary–single interactions (model M12), the angular momentum direction of binaries typically remains unchanged from the initial direction. In this case, it is aligned (or antialigned) with the AGN disk angular momentum direction with a probability of 0.5, which limits the efficient production of positive $\chi_{\rm eff}$.

However, models characterized by rapid accretion (models M19–M20) and by high gas density (model M13) show a correlation between q and the average of $\chi_{\rm eff}$. This correlation arises from the enhancement of $\chi_{\rm eff}$ driven by spin alignment through accretion due to the Bardeen–Petterson effect, the asymmetric mass ratios resulting from mergers across different generation BHs (such as mergers between first- and second-generation BHs), and spin enhancements due to mergers. Note that while mass and spin growth through accretion contribute to a positive correlation, mass growth from hierarchical mergers leads to a negative correlation by producing asymmetric mass ratio mergers. Although alignment due to accretion is required for the negative correlation, the growth of mass and spin magnitude should be predominantly driven by mergers, with accretion playing a minor role.

Figure 14 also shows the q–$\chi_{\rm eff}$ correlation and the distribution of individual mergers for model M20. Mergers between first- and second-generation BHs are typically clustered around $q \sim 0.4$–0.7 (red points), while mergers involving third- or higher-generation BHs contribute to $q \gtrsim 0.1$ (purple points). Here, we define an nth-generation BH as one composed of n first-generation BHs. These results imply that hierarchical mergers with efficient alignment via gas accretion can produce a negative correlation between the average of $\chi_{\rm eff}$ and q. Moreover, high-generation mergers generally have large $\chi_{\rm eff}$, consistent with Y.-J. Li et al. (2026a). Thus, in the AGN channel, it is possible to generate a negative correlation between q and the mean $\chi_{\rm eff}$, providing a promising observational signature of this model.

Similarly, a negative correlation between q and the spin magnitude is suggested by A. Vijaykumar et al. (2026). This correlation can be produced by hierarchical mergers in most models, unless gas accretion is efficient and significantly enhances q values, as seen in model M19.

On the other hand, The LIGO Scientific Collaboration et al. (2026b) suggested that by analyzing a larger number of GW events and using a more flexible model, the confidence level for the negative correlation between q and the average of $\chi_{\rm eff}$ is reduced to 82% credibility, while the negative correlation between q and the dispersion of $\chi_{\rm eff}$ is found to have 95% credibility. This correlation between q and the dispersion of $\chi_{\rm eff}$ is clearly observed in most models, except for model M1 at $t = 30$ Myr and model M19. This correlation is driven by hierarchical mergers, which result in high BH spin magnitude and low q (if the generations of merging BHs are different), leading to mergers characterized by low q and high dispersion of $\chi_{\rm eff}$. Since the efficient accretion likely diminishes this correlation, this comparison is useful for constraining the accretion process.

If the negative correlation between q and the average of $\chi_{\rm eff}$ is real, a model characterized by efficient accretion and hierarchical mergers, such as model M20, is favored (Figures 13 and 14). This model also produces a positive correlation between m_1 and the average of $\chi_{\rm eff}$ (Figure 12), as suggested by Y.-J. Li et al. (2026b). Since this positive correlation is well reproduced only by highly accreting models (models M19 and M20) while the model with the most efficient accretion (model M19) fails to reproduce the mass distribution, we tentatively regard model M20 as the most promising model. A potential problem is that the average of $|\chi_{\rm eff}|$ at high $M_{\rm chirp}$ appears larger than the observational median; if this constraint tightens to around the current median values, a model with less efficient accretion (e.g., model M1) would be preferred. Further observations and analyses will help discriminate between these models.

Several studies have reproduced the q–$\chi_{\rm eff}$ correlation via the AGN channel (B. McKernan et al. 2022; B. McKernan & K. E. S. Ford 2024; H. E. Cook et al. 2025; B. McKernan et al. 2025), although notable differences remain relative to our model. B. McKernan et al. (2022) and B. McKernan & K. E. S. Ford (2024) explained that this correlation arises because massive BHs tend to be rapidly captured by the AGN disk and spun up more efficiently, enabling mergers with lower-mass massive BHs that retain random spins. Meanwhile, B. McKernan et al. (2025) and H. E. Cook et al. (2025) interpret the correlation in terms of spin alignment and hierarchical mergers; however, their resulting distributions differ significantly from those in our model, particularly the presence of bimodal peaks in $\chi_{\rm eff}$. These differences likely stem from several modeling choices in those works: no treatment of binary component exchanges or evolution of angular momentum directions during binary–single interactions; the assumption that the circumbinary disk is always aligned with the AGN disk regardless of the binary's angular momentum; a fixed capture rate from the nuclear star cluster; a fixed hardening time of binaries due to gaseous torques in the unit of orbital timescale around the SMBH; no inclination excitation of kicked objects; and the assumption that binaries form whenever two BHs come within the Hill radius (B. McKernan et al. 2022, 2025; H. E. Cook et al. 2025). Additionally, other channels involving isolated binary

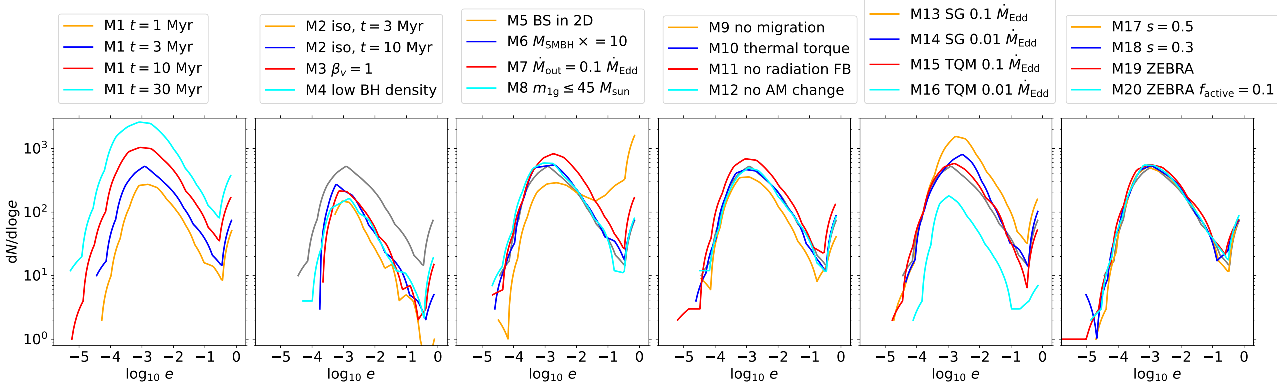

Figure 15. The linearly interpolated distribution of the orbital eccentricity of merging binaries for models M1–M20.

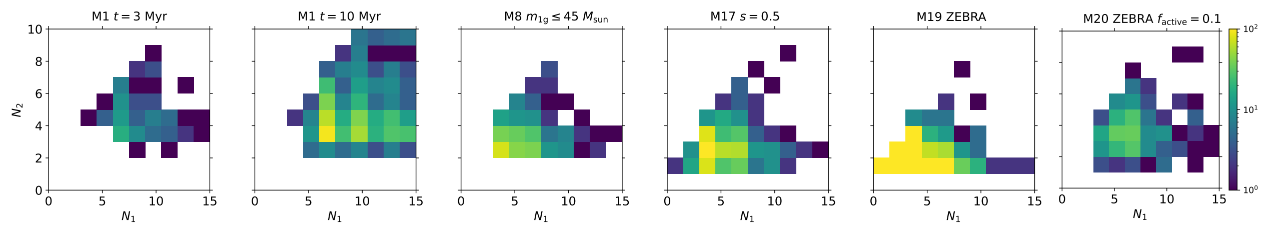

Figure 16. The distribution of the number of generations composing the primary and secondary BHs in mergers among massive BHs ($m_1 \geqslant 100\,M_{\odot}$ and $m_2 \geqslant 50\,M_{\odot}$). To reduce Poisson noise, we performed 100 simulations.

evolution have been proposed to produce similar correlations (M. Zevin & S. S. Bavera 2022; A. Olejak et al. 2024; S. Banerjee & A. Olejak 2026; Z.-Y. Wang et al. 2026b). However, to generate high $\chi_{\rm eff}$ values preferentially for massive BHs, as suggested by Y.-J. Li et al. (2026a), the AGN scenario is likely more favorable.

3.1.5. Eccentricity

Figure 15 shows the distribution of eccentricities at 10 Hz. In the fiducial model, the eccentricity at this frequency is distributed at around $e_{10\rm Hz} \sim 10^{-4}$–0.1 for mergers of binaries formed through gas-capture processes, three-body interactions, and primordial binaries. Nonzero eccentricities around $e \sim 10^{-3}$ are characterized by the competition between hardening due to gas dynamical friction and GW emission (with high initial values established during binary–single interactions or binary formation). Conversely, the highest eccentricities of $e_{10\rm Hz} \gtrsim 0.1$ are primarily contributed by highly eccentric binaries formed through GWC processes (H. Tagawa et al. 2021b; L. Gondán & B. Kocsis 2022; J. Samsing et al. 2022). This process typically occurs during binary–single interactions. The minimum value of the eccentricity resulting from the GWC mechanism (∼0.1) is determined by the relative velocity of the binary–single interactions (e.g., G. D. Quinlan & S. L. Shapiro 1989), which depends on the semimajor axis of the binaries before the interactions. As demonstrated in previous studies (H. Tagawa et al. 2021b; I. Romero-Shaw et al. 2025), the eccentricity distribution is sensitive to the treatment of binary–single interactions (model M5, indicated by the orange line in the second panel), which significantly influences the merger rate through GWC processes.

Notably, highly eccentric mergers are prevalent in these models (model M5). Approximately one-half of the mergers exhibit $e_{10\rm Hz} \gtrsim 0.4$, compared to those with $e_{10\rm Hz} \gtrsim 0.1$, as discussed in I. Romero-Shaw et al. (2025). Such highly eccentric mergers may correspond to several events with $e_{10\rm Hz} \gtrsim 0.4$, as suggested by Y. Xu et al. (2026). Given the difficulty of producing these highly eccentric mergers from typical interactions in gas-poor environments, they may serve as a promising signature of mergers occurring within AGN disks (but see A. Rasskazov & B. Kocsis 2019; L. Gondán & B. Kocsis 2022).

3.2. Massive Mergers

Reflecting the findings of massive BH mergers, such as GW190521 and GW231123, we investigate whether mergers with similar properties can be produced via the AGN channel. For GW190521 (R. Abbott et al. 2020), the parameters are $m_1 = 85^{+21}_{-14}\,M_{\odot}$, $m_2 = 66^{+17}_{-18}\,M_{\odot}$, $\chi_{\rm eff} = 0.08^{+0.27}_{-0.36}$, $\chi_{\rm p} = 0.68^{+0.25}_{-0.37}$, $a_1 = 0.69^{+0.27}_{-0.62}$, and $a_2 = 0.73^{+0.24}_{-0.64}$. For GW231123 (A. G. Abac et al. 2025a), the parameters are $m_1 = 137^{+22}_{-17}\,M_{\odot}$, $m_2 = 103^{+20}_{-52}\,M_{\odot}$, $\chi_{\rm eff} = 0.31^{+0.24}_{-0.39}$, $\chi_{\rm p} = 0.77^{+0.17}_{-0.19}$, $a_1 = 0.90^{+0.10}_{-0.19}$, and $a_2 = 0.80^{+0.20}_{-0.51}$. These massive mergers are characterized by high spin magnitudes and strong spin precession. Several studies discussed whether these masses (S. Goyal et al. 2025; B. Liu & D. Lai 2025; S. Liu et al. 2025; L. Paiella et al. 2025; X. Shan et al. 2025; Chakraborty & S. Mukherjee 2026; A. Y.-J. Li et al. 2026a; A. Tanikawa et al. 2026; Q. Yang et al. 2026) and/or spins (V. Delfavero et al. 2025; O. Gottlieb et al. 2025; S. A. Popa & S. E. de Mink 2025; J. Stegmann et al. 2025; I. Bartos & Z. Haiman 2026; D. Croon et al. 2026; V. De Luca et al. 2026; L. Passenger et al. 2026) can be explained by various models.

Focusing on massive BH mergers, Figures 16, 17, 18, 19, and 20 show the distributions of properties for mergers involving a primary BH with $m_1 \geqslant 100\,M_{\odot}$ and a secondary BH with $m_2 \geqslant 50\,M_{\odot}$. In Figures 4 and 16, respectively, the merging masses and the generations of high-mass mergers are shown for models M1 (at $t = 3$ and 10 Myr), M8, M17, M19, and M20. These models were selected because their merging-

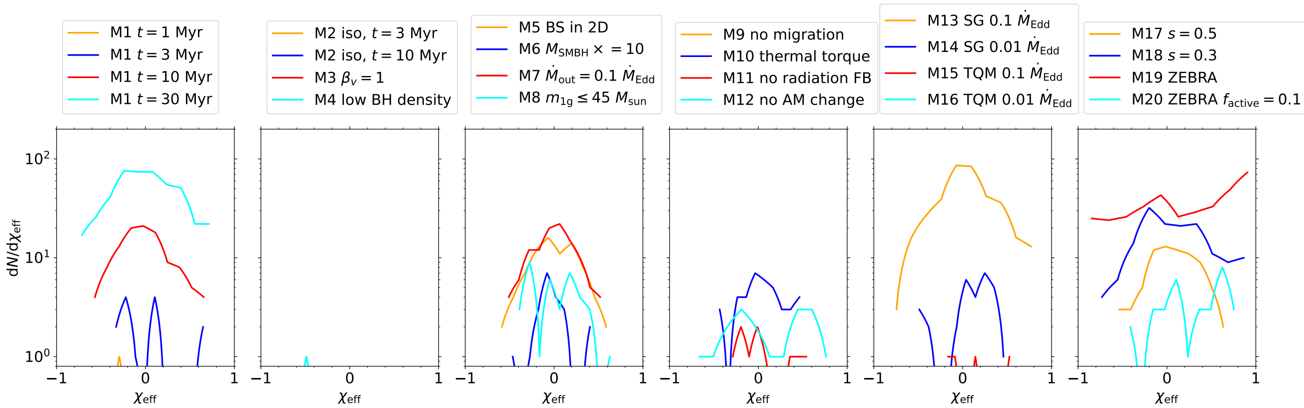

Figure 17. The linearly interpolated distribution of $\chi_{\rm eff}$ for mergers among massive BHs.

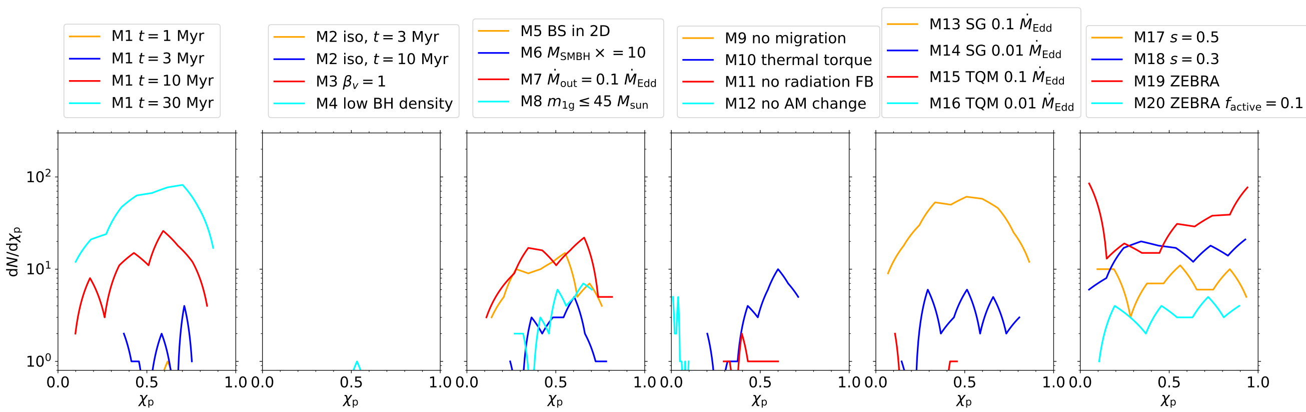

Figure 18. The linearly interpolated distribution of $\chi_{\rm p}$ for mergers among massive BHs.

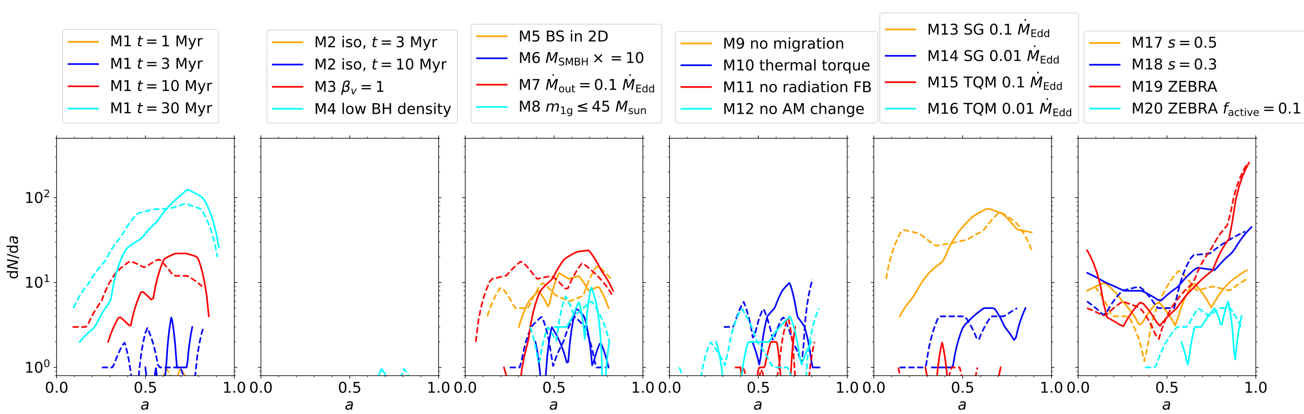

Figure 19. The linearly interpolated distribution of the spin magnitude of merging binaries composed of massive BHs. Solid and dashed lines represent distributions of the spin magnitudes of the primary and secondary BHs, respectively.

mass distributions typically differ (e.g., Figures 2–3). For models M1 and M20, massive mergers occur among ∼fifth- to tenth-generation BHs, consistent with the model of Y.-J. Li et al. (2026a). In model M8, where the initial BH mass is higher than in the fiducial model, massive mergers primarily involve ∼fifth-generation BHs. Additionally, in models M17 and M19, where accretion is more efficient, mergers among low-generation ($\lesssim$fifth) BHs contribute significantly to the high-mass mergers, in line with the suggestions of I. Bartos & Z. Haiman (2026). On the other hand, in models with short duration (model M1 at $t = 1$ Myr), a small number of BHs in AGN disks (models M2–M4), no migration (model M9), or low gas density (models M15 and M16), massive mergers like those found in GW231123 are difficult to produce.

Figures 17, 18, and 19 show, respectively, the distributions of $\chi_{\rm eff}$, $\chi_{\rm p}$, and BH spin magnitudes for massive mergers across models M1–M20. The distribution of $\chi_{\rm eff}$ around ∼0 in many models (Figure 17) results from the frequent randomization of angular momentum directions due to binary–single interactions.

In models M17–M19, where accretion is significant, the spin magnitudes of massive BHs are distributed over a wide range of values instead of being concentrated around $a \sim 0.7$ (Figure 19). Moreover, θ_{a-l} tends to decrease in these models,

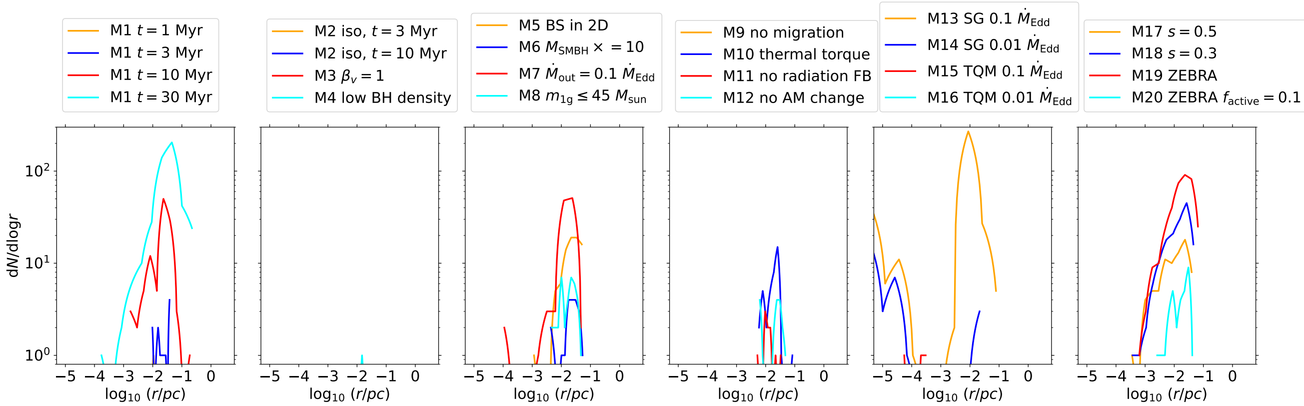

Figure 20. The linearly interpolated distribution of the distance from the SMBH of the mergers among massive BHs.

leading to lower χ_p values (Figure 18), although θ_{a-l} is still distributed over a wide range. Consequently, these models can readily produce the high spin magnitude and χ_p suggested for GW231123. By contrast, when accretion is inefficient, as prescribed in the fiducial and many other models, the probability of producing spins $\gtrsim 0.7$ is lower. L. Passenger et al. (2026) estimate that, in globular clusters, where up to second generation–second generation mergers can occasionally occur, there is only an $\sim$1% chance that merger-remnant spins are consistent with those inferred for GW231123. Nevertheless, since higher-generation BHs tend to have larger spins (A. Borchers et al. 2025), BHs with spins consistent with GW231123 could still arise from mergers among higher-generation objects in the fiducial model.

Figure 20 shows the distribution of the distance from the SMBH at which massive BH mergers occur. Most mergers primarily peak around 0.01–0.05 pc from the SMBH, with no peak at $\sim$3 pc unlike for low-mass mergers, consistent with the locations of hierarchical mergers as opposed to mergers of primordial binaries (see Figure 6).

Overall, massive BH mergers, such as GW231123, can be produced by hierarchical mergers among $\sim$third- to tenth-generation BHs or through efficient accretion. In the former case, the BH spins are typically distributed around $\sim$0.7, while in the latter case, the BH spins tend to be closer to one.

4. Conclusions

We have thoroughly investigated the properties of BH mergers in AGN disks for a broad range of model parameters and prescriptions. To calculate the distribution of observables, we use 1D N-body simulations combined with a semianalytical model. Our findings are summarized as follows.

1. In our fiducial model, the distributions of masses and mass ratios are similar to those observed by LVK. However, they depend strongly on the lifetime and density of the AGN disk and on the number and accretion efficiency of BHs, with higher masses predicted as these quantities increase.
2. The negative correlation between q and the average of $\chi_{\rm eff}$, as suggested by observed GW events, can arise in a model with efficient gas accretion and hierarchical mergers. In such a model, higher-generation BHs produce a high spin magnitude and low q (if the generations of merging BHs are different). Additionally, accretion reduces the angle between BH spins and the angular momentum direction of the binaries, resulting in mergers characterized by high $\chi_{\rm eff}$. On the other hand, the negative correlation between q and the dispersion of $\chi_{\rm eff}$, which is estimated to be more significant, can arise in most models due to hierarchical mergers, provided that gas accretion is not overly efficient.
3. The positive correlation between $\chi_{\rm eff}$ and $M_{\rm chirp}$ reported in recent GW analyses can be reproduced if accretion onto BHs is efficient. Accordingly, the model with moderately efficient accretion (model M20) appears to be overall the most promising for explaining the observations, whereas the model with highly efficient accretion (model M19) is unlikely, as it overproduces the high $M_{\rm chirp}$ tail.
4. The positive correlation between the effective spin magnitude $|\chi_{\rm eff}|$ (instead of $\chi_{\rm eff}$ above) and $M_{\rm chirp}$ can be reproduced by hierarchical mergers, which can help constrain the properties of first-generation BHs, accretion processes, and the interactions between BHs.
5. In the fiducial model, mergers frequently occur in the outer regions ($\gtrsim$parsec) due to the abundance of preexisting binaries in these regions, as well as in the inner regions around $\sim$0.01–0.05 pc from the SMBH where capture into an AGN disk and gas-capture binary formation are efficient. The merger location and binary formation processes are further influenced by the AGN disk models utilized.
6. The eccentricity distribution at merger is predominantly influenced by the geometry of binary–single interactions (either isotropic or 2D coplanar with the AGN disk), as the probability of the GWC process is sensitive to this geometry.
7. Massive mergers as observed in GW231123 can be produced either through hierarchical mergers among $\geqslant$third-generation BHs or via low-generation mergers with efficient gas accretion. In the former case, the BH spin is typically distributed around $\sim$0.7, while in the latter case, it is closer to $\sim$1.

Based on all of the above, we tentatively regard model M20 to be the most promising model overall. This model effectively reproduces the negative correlation between q and the average of $\chi_{\rm eff}$, as well as a positive correlation between m_1 and the average of $\chi_{\rm eff}$. Both correlations highlight the necessity for efficient accretion and hierarchical mergers. However, a potential concern may arise regarding the average of $|\chi_{\rm eff}|$ at high $M_{\rm chirp}$, which seems to exceed the observational median. If this constraint tightens to align more closely with the current median values, a model with less efficient accretion, such as model M1, would be favored to prevent excessive spin growth and alignment due to accretion. Given the parameter dependencies demonstrated in this work, further observations and more dedicated analyses (e.g., L. Xue et al. 2025; V. Gayathri et al. 2025, for N parameter cases) will be crucial for deriving a formal best-fit model in future studies.

Further modeling that includes various components and their interactions, the evolution of AGN disks, and a realistic treatment of processes using N-body and hydrodynamical simulations would be valuable for improving predictions. Additionally, the identification of possible electromagnetic counterparts would enhance our understanding of their evolution.

Acknowledgments

H.T. is supported by the National Science and Technology Major Project of China (No. 2024ZD1100601) and the National Key R&D Program of China (grant No.2024YFC2207700). Z.H. was supported by NASA grants 80NSSC22K0822 and 80NSSC24K0440. B.K. is supported by the Science and Technology Facilities Council grant No. ST/W000903/1. Simulations were carried out on Cray XD2000 at the Center for Computational Astrophysics, National Astronomical Observatory of Japan.

ORCID iDs

Hiromichi Tagawa https://orcid.org/0000-0002-5674-0644
Zoltán Haiman https://orcid.org/0000-0003-3633-5403
Bence Kocsis https://orcid.org/0000-0002-4865-7517

References

Aarseth, S. J., & Heggie, D. C. 1976, A&A, 53, 259
Abac, A. G., Abouelfettouh, I., Acernese, F., et al. 2025a, ApJL, 993, L25
Abac, A. G., Abouelfettouh, I., Acernese, F., et al. 2025b, ApJL, 993, L21
Abbott, R., Abbott, T. D., Abraham, S., et al. 2020, PhRvL, 125, 101102
Acernese, F., Agathos, M., Agatsuma, K., et al. 2015, CQGra, 32, 024001
Adamcewicz, C., Guttman, N., Lasky, P. D., & Thrane, E. 2025, ApJ, 994, 261
Adamcewicz, C., Lasky, P. D., & Thrane, E. 2023, ApJ, 958, 13
Adamcewicz, C., & Thrane, E. 2022, MNRAS, 517, 3928
Akutsu, T., Ando, M., Arai, K., et al. 2021, PTEP, 2021, 05A101
Alexander, T., & Hopman, C. 2009, ApJ, 697, 1861
Antonini, F., Rodriguez, C. L., Petrovich, C., & Fischer, C. L. 2018, MNRAS, 480, L58
Antonini, F., Romero-Shaw, I. M., & Callister, T. 2025, PhRvL, 134, 011401
Antonini, F., Toonen, S., & Hamers, A. S. 2017, ApJ, 841, 77
Arca Sedda, M. 2020, ApJ, 891, 47
Arca-Sedda, M., & Capuzzo-Dolcetta, R. 2014, MNRAS, 444, 3738
Ashton, G., Ackley, K., Hernandez, I. M., & Piotrzkowski, B. 2021, CQGra, 38, 235004
Bagoly, Z., Szécsi, D., Balázs, L. G., et al. 2016, A&A, 593, L10
Banerjee, S. 2017, MNRAS, 524, 467
Banerjee, S., & Olejak, A. 2026, OJAp, 9
Barausse, E., Morozova, V., & Rezzolla, L. 2012, ApJ, 758, 63
Bartko, H., Martins, F., Trippe, S., et al. 2010, ApJ, 708, 834
Bartos, I., & Haiman, Z. 2026, ApJL, 996, L44
Bartos, I., Haiman, Z., Marka, Z., et al. 2017a, NatCo, 8, 831
Bartos, I., Kocsis, B., Haiman, Z., & Márka, S. 2017b, ApJ, 835, 165
Begelman, M. C., & Volonteri, M. 2017, MNRAS, 464, 1102
Belczynski, K., Daniel, E. H., Bulik, T., & O'Shaughnessy, R. 2016, Natur, 534, 512
Bell, K. R., & Lin, D. N. C. 1994, ApJ, 427, 987
Bellovary, J. M., Mac Low, M.-M., McKernan, B., & Ford, K. E. S. 2016, ApJL, 819, L17
Binney, J., & Tremaine, S. 2008, Galactic Dynamics (2nd ed.; Princeton Univ. Press)
Blandford, R. D., & Begelman, M. C. 1999, MNRAS, 303, L1
Boekholt, T. C. N., Rowan, C., & Kocsis, B. 2023, MNRAS, 518, 5653
Borchers, A., Ye, C. S., & Fishbach, M. 2025, ApJ, 987, 146
Calcino, J., Dempsey, A. M., Dittmann, A. J., & Li, H. 2024, ApJ, 970, 107
Calderón Bustillo, J., Leong, S. H. W., Chandra, K., McKernan, B., & Ford, K. E. S. 2021, arXiv:2112.12481
Callister, T. A., Haster, C.-J., Ng, K. K. Y., Vitale, S., & Farr, W. M. 2021, ApJL, 922, L5
Chakraborty, A., & Mukherjee, S. 2026, ApJ, 1003, 20
Chatzopoulos, E., & Wheeler, J. C. 2012, ApJ, 748, 42
Chen, K., & Dai, Z.-G. 2024, ApJ, 961, 206
Chen, K., & Dai, Z.-G. 2025, ApJ, 987, 214
Chen, Y.-X., Bailey, A., Stone, J., & Zhu, Z. 2022, ApJL, 939, L23
Chen, Y.-X., Jiang, Y.-F., Goodman, J., & Ostriker, E. C. 2023, ApJ, 948, 120
Collin, S., & Zahn, J.-P. 2008, A&A, 477, 419
Colloms, S., Doctor, Z., & Berry, C. P. L. 2025, ApJ, 995, 123
Connaughton, V., Burns, E., Goldstein, A., et al. 2016, ApJL, 826, L6
Connaughton, V., Burns, E., Goldstein, A., et al. 2018, ApJL, 853, L9
Cook, H. E., McKernan, B., Ford, K. E. S., et al. 2025, ApJ, 993, 163
Corley, K. R., Bartos, I., Singer, L. P., et al. 2019, MNRAS, 488, 4459
Coughlin, E. R., & Begelman, M. C. 2014, ApJ, 781, 82
Croon, D., Gerosa, D., & Sakstein, J. 2026, MNRAS, 546, stag073
De Luca, V., Franciolini, G., & Riotto, A. 2026, PhRvL, 136, 201401
DeLaunay, J., Tohuvavohu, A., Ronchini, S., et al. 2024, GCN, 38351, 1
DeLaurentiis, S., Epstein-Martin, M., & Haiman, Z. 2023, MNRAS, 523, 1126
Delfavero, V., Ray, S., Cook, H. E., et al. 2025, arXiv:2508.13412
Dempsey, A. M., Li, H., Mishra, B., & Li, S. 2022, ApJ, 940, 155
Derdzinski, A., & Mayer, L. 2023, MNRAS, 521, 4522
Derdzinski, A. M., D'Orazio, D., Duffell, P., Haiman, Z., & MacFadyen, A. 2019, MNRAS, 486, 2754
Dittmann, A. J., Dempsey, A. M., & Li, H. 2024, ApJ, 964, 61
Dittmann, A. J., Dempsey, A. M., & Li, H. 2025, ApJ, 990, 137
Do, T., Kerzendorf, W., Konopacky, Q., et al. 2018, ApJL, 855, L5
Dodici, M., & Tremaine, S. 2024, ApJ, 972, 193
Dominik, M., Belczynski, K., Fryer, C., et al. 2012, ApJ, 759, 52
Duffell, P. C., Haiman, Z., MacFadyen, A. I., D'Orazio, D. J., & Farris, B. D. 2014, ApJL, 792, L10
Epstein-Martin, M., Stone, N., & Becker, J. 2025a, arXiv:2510.12895
Epstein-Martin, M., Tagawa, H., Haiman, Z., & Perna, R. 2025b, MNRAS, 537, 3396
Fabj, G., Tiede, C., Rowan, C., Pessah, M., & Samsing, J. 2026, MNRAS, 547, stag427
Fahrion, K., Leaman, R., Lyubenova, M., & van de Ven, G. 2022, A&A, 658, A172
Fahrion, K., Lyubenova, M., van de Ven, G., et al. 2021, A&A, 650, A137
Farah, A. M., Vijaykumar, A., & Fishbach, M. 2026, ApJL, 1001, L40
Feldmeier, A., Neumayer, N., Seth, A., et al. 2014, A&A, 570, A2
Ford, K. E. S., & McKernan, B. 2022, MNRAS, 517, 5827
Fragile, P. C., Middleton, M. J., Bollimpalli, D. A., & Smith, Z. 2025, MNRAS, 540, 2820
Fragione, G., Grishin, E., Leigh, N. W. C., Perets, H. B., & Perna, R. 2019, MNRAS, 488, 47
Fragione, G., & Kocsis, B. 2019, MNRAS, 486, 4781
Freitag, M., Amro-Seoane, P., & Kalogera, V. 2006, ApJ, 649, 91
Gamba, R., Breschi, M., Carullo, G., et al. 2023, NatAs, 7, 11
Gangardt, D., Trani, A. A., Bonnerot, C., & Gerosa, D. 2024, MNRAS, 530, 3689
Gayathri, V., Healy, J., Lange, J., et al. 2022, NatAs, 6, 344
Gayathri, V., Yang, Y., Tagawa, H., Haiman, Z., & Bartos, I. 2021, ApJL, 920, L42
Gayathri, V., Iorio, G., Tagawa, H., et al. 2025, arXiv:2509.09647
Generozov, A., & Perets, H. B. 2023, MNRAS, 522, 1763
Genzel, R., Eisenhauer, F., & Gillessen, S. 2010, RvMP, 82, 3121
Ghez, A. M., Salim, S., Weinberg, N. N., et al. 2008, ApJ, 689, 1044
Gilbaum, S., Grishin, E., Stone, N. C., & Mandel, I. 2025, ApJL, 982, L13
Gilbaum, S., & Stone, N. C. 2022, ApJ, 928, 191
Ginat, Y. B., & Perets, H. B. 2021, PhRvX, 11, 031020
Ginat, Y. B., & Perets, H. B. 2023, MNRAS, 519, L15
Goldreich, P., Lithwick, Y., & Sari, R. 2002, Natur, 420, 643
Gondán, L., & Kocsis, B. 2022, MNRAS, 515, 3299
Goodman, J., & Tan, J. C. 2004, ApJ, 608, 108
Gottlieb, O., Metzger, B. D., Issa, D., et al. 2025, ApJL, 993, L54
Goyal, S., Villarrubia-Rojo, H., & Zumalacarregui, M. 2025, arXiv:2512.17631
Graham, M. J., Ford, K. E. S., McKernan, B., et al. 2020, PhRvL, 124, 251102
Graham, M. J., McKernan, B., Ford, K. E. S., et al. 2023, ApJ, 942, 99

Gravity Collaboration, Abuter, R., Amorim, A., et al. 2020, A&A, 636, L5
Greene, J. E., & Ho, L. C. 2007, ApJ, 667, 131
Grishin, E., Gilbaum, S., & Stone, N. C. 2024, MNRAS, 530, 2114
Gröbner, M., Ishibashi, W., Tiwari, S., Haney, M., & Jetzer, P. 2020, A&A, 638, A119
Gupte, N., Ramos-Buades, A., Buonanno, A., et al. 2025, PhRvD, 112, 104045
Gupte, N., Miller, M. C., Udall, R., et al. 2026, arXiv:2603.29019
Guttman, N., Payne, E., Lasky, P. D., & Thrane, E. 2026, ApJ, 996, 144
Hankla, A. M., Jiang, Y.-F., & Armitage, P. J. 2020, ApJ, 902, 50
Heggie, D. C. 1975, MNRAS, 173, 729
Hendriks, K., Zwick, L., Saini, P., Takátsy, J., & Samsing, J. 2026, arXiv:2601.14918
Hendriks, K., Atallah, D., Martinez, M., et al. 2024, arXiv:2411.08572
Hoang, B.-M., Naoz, S., Kocsis, B., Rasio, F. A., & Dosopoulou, F. 2018, ApJ, 856, 140
Hopkins, P. F., Baron, D., & Piotrowska, J. M. 2026, OJAp, doi:10.33232/001c.161388
Hopkins, P. F., Grudic, M. Y., Su, K.-Y., et al. 2024, OJAp, 7, 18
Hopman, C., & Alexander, T. 2006, ApJL, 645, L133
Hu, H., Inayoshi, K., Haiman, Z., et al. 2022, ApJ, 935, 140
Inayoshi, K., Tamanini, N., Caprini, C., & Haiman, Z. 2017, PhRvD, 96, 063014
Ishibashi, W., & Gröbner, M. 2024, MNRAS, 529, 883
Jiang, Y.-F., Davis, S. W., & Stone, J. M. 2016, ApJ, 827, 10
Kaaz, N., Schrøder, S. L., Andrews, J. J., Antoni, A., & Ramirez-Ruiz, E. 2023, ApJ, 944, 44
Kanagawa, K. D., Muto, T., Tanaka, H., et al. 2015, ApJL, 806, L15
Kanagawa, K. D., Tanaka, H., & Szuszkiewicz, E. 2018, ApJ, 861, 140
Kato, S., Fukue, J., & Mineshige, S. 2008, Black-Hole Accretion Disks—Towards a New Paradigm (Kyoto Univ. Press)
King, A. R., Pringle, J. E., & Livio, M. 2007, MNRAS, 376, 1740
Kinugawa, T., Inayoshi, K., Hotokezaka, K., Nakauchi, D., & Nakamura, T. 2014, MNRAS, 442, 2963
Kıroğlu, F., Kremer, K., Biscoveanu, S., González Prieto, E., & Rasio, F. A. 2025a, ApJ, 979, 237
Kıroğlu, F., Lombardi, J. C., Kremer, K., Vanderzyden, H. D., & Rasio, F. A. 2025b, ApJL, 983, L9
Kremer, K., Ye, C. S., Rui, N. Z., et al. 2020, ApJS, 247, 48
Kumamoto, J., Fujii, M. S., & Tanikawa, A. 2019, MNRAS, 486, 3942
Leigh, N. W. C., Geller, A. M., McKernan, B., et al. 2018, MNRAS, 474, 5672
Levin, Y., & Beloborodov, A. M. 2003, ApJL, 590, L33
Li, J., Dempsey, A. M., Li, H., Lai, D., & Li, S. 2023, ApJL, 944, L42
Li, J., Lai, D., & Rodet, L. 2022a, ApJ, 934, 154
Li, R., & Lai, D. 2022, MNRAS, 517, 1602
Li, R., & Lai, D. 2023, MNRAS, 522, 1881
Li, R., & Lai, D. 2024, MNRAS, 529, 348
Li, Y.-J., Tang, S.-P., Xue, L.-Q., & Fan, Y.-Z. 2026a, ApJ, 999, 127
Li, Y.-J., Wang, Y.-Z., Tang, S.-P., Chen, T., & Fan, Y.-Z. 2025, ApJ, 987, 65
Li, Y.-J., Wang, Y.-Z., Tang, S.-P., & Fan, Y.-Z. 2024, PhRvL, 133, 051401
Li, Y.-J., Wang, Y.-Z., Tang, S.-P., & Fan, Y.-Z. 2026b, PhRvL, 137, 021407
Li, Y.-P., Chen, Y.-X., Lin, D. N. C., & Wang, Z. 2022b, ApJL, 928, L1
Li, Y.-P., Dempsey, A. M., Li, H., Li, S., & Li, J. 2022c, ApJL, 928, L19
Li, Y.-P., Dempsey, A. M., Li, S., Li, H., & Li, J. 2021, ApJ, 911, 124
LIGO Scientific Collaboration, Aasi, J., Abbott, B. P., et al. 2015, CQGra, 32, 074001
Liu, B., & Lai, D. 2025, arXiv:2511.13820
Liu, S., Wang, L., Tanikawa, A., Wu, W., & Fujii, M. S. 2025, ApJL, 993, L30
Lodato, G., & Gerosa, D. 2013, MNRAS, 429, L30
Lousto, C. O., Zlochower, Y., Dotti, M., & Volonteri, M. 2012, PhRvD, 85, 084015
Lu, J. R., Do, T., Ghez, A. M., et al. 2013, ApJ, 764, 155
Lubow, S. H., Seibert, M., & Artymowicz, P. 1999, ApJ, 526, 1001
Ma, Z.-P., Wang, K., Wu, Q., & Wang, J.-M. 2025, PhRvD, 111, 083033
Madau, P., & Dickinson, M. 2014, ARA&A, 52, 415
Martini, P. 2004, Coevolution of Black Holes and Galaxies (Cambridge Univ. Press), 169
Masset, F. S. 2017, MNRAS, 472, 4204
McKernan, B., & Ford, K. E. S. 2024, MNRAS, 531, 3479
McKernan, B., Ford, K. E. S., Callister, T., et al. 2022, MNRAS, 514, 3886
McKernan, B., Ford, K. E. S., O'Shaugnessy, R., & Wysocki, D. 2020, MNRAS, 494, 1203
McKernan, B., Ford, K. E. S., Bartos, I., et al. 2019, ApJL, 884, L50
McKernan, B., Ford, K. E. S., Bellovary, J., et al. 2018, ApJ, 866, 66
McKernan, B., Ford, K. E. S., Cook, H. E., et al. 2025, ApJ, 990, 217
Meiron, Y., Kocsis, B., & Loeb, A. 2017, ApJ, 834, 200
Milosavljević, M., & Loeb, A. 2004, ApJL, 604, L45
Miralda-Escudé, J., & Kollmeier, J. A. 2005, ApJ, 619, 30
Moncrieff, J. W. N., Grishin, E., Trani, A. A., Panther, F. H., & Pietrosanti, O. 2026, MNRAS, 545, staf2217
Moncrieff, J. W. N., & Panther, F. H. 2025, MNRAS, 543, 1833
Moody, M. S. L., Shi, J.-M., & Stone, J. M. 2019, ApJ, 875, 66
Morras, G., Pratten, G., & Schmidt, P. 2026, ApJL, 1000, L2
Morton, S. L., Rinaldi, S., Torres-Orjuela, A., et al. 2023, PhRvD, 108, 123039
Nayakshin, S., Cuadra, J., & Springel, V. 2007, MNRAS, 379, 21
Ogilvie, G. I. 1999, MNRAS, 304, 557
O'Leary, R. M., Kocsis, B., & Loeb, A. 2009, MNRAS, 395, 2127
O'Leary, R. M., Meiron, Y., & Kocsis, B. 2016, ApJL, 824, L12
Olejak, A., Klencki, J., Xu, X.-T., et al. 2024, A&A, 689, A305
Ostriker, J. P. 1983, ApJ, 273, 99
Paiella, L., Ugolini, C., Spera, M., Branchesi, M., & Arca Sedda, M. 2025, ApJL, 994, L54
Palmese, A., Fishbach, M., Burke, C. J., Annis, J., & Liu, X. 2021, ApJL, 914, L34
Pan, Z., & Yang, H. 2021a, PhRvD, 103, 103018
Pan, Z., & Yang, H. 2021b, ApJ, 923, 173
Passenger, L., Banagiri, S., Thrane, E., et al. 2026, ApJ, 999, 236
Peng, P., & Chen, X. 2021, MNRAS, 505, 1324
Peters, P. C. 1964, PhRv, 136, 1224
Pfuhl, O., Alexander, T., & Gillessen, S. 2014, ApJ, 782, 101
Pierra, G., Mastrogiovanni, S., & Perriès, S. 2024, A&A, 692, A80
Planas, M. d. L., Ramos-Buades, A., García-Quirós, C., et al. 2025, PhRvD, 112, 123004
Plunkett, C., Callister, T., Zevin, M., & Vitale, S. 2026, PhRvL, 2, 021404
Popa, S. A., & de Mink, S. E. 2025, ApJL, 995, L76
Portegies Zwart, S. F., & McMillan, S. L. W. 2000, ApJL, 528, L17
Poutanen, J., Lipunova, G., Fabrika, S., Butkevich, A. G., & Abolmasov, P. 2007, MNRAS, 377, 1187
Qian, K., Li, J., & Lai, D. 2024, ApJ, 962, 143
Quinlan, G. D., & Shapiro, S. L. 1989, ApJ, 343, 725
Rasskazov, A., & Kocsis, B. 2019, ApJ, 881, 20
Rastello, S., Amaro-Seoane, P., Arca-Sedda, M., et al. 2019, MNRAS, 483, 1233
Rezzolla, L., Barausse, E., Dorband, E. N., et al. 2008, PhRvD, 78, 044002
Rodriguez, C. L., Amaro-Seoane, P., Chatterjee, S., et al. 2018, PhRvD, 98, 123005
Rodriguez, C. L., & Antonini, F. 2018, ApJ, 863, 7
Rodriguez, C. L., Chatterjee, S., & Rasio, F. A. 2016, PhRvD, 93, 084029
Rodríguez-Ramírez, J. C., Bom, C. R., Fraga, B., & Nemmen, R. 2024, MNRAS, 527, 6076
Rodríguez-Ramírez, J. C., Nemmen, R., & Bom, C. R. 2025, PhRvD, 111, 083020
Romero-Shaw, I., Lasky, P. D., & Thrane, E. 2022, ApJ, 940, 171
Romero-Shaw, I., Lasky, P. D., Thrane, E., & Calderón Bustillo, J. 2020, ApJL, 903, L5
Romero-Shaw, I., Stegmann, J., Tagawa, H., et al. 2025, PhRvD, 112, 063052
Romero-Shaw, I. M., Gerosa, D., & Loutrel, N. 2023, MNRAS, 519, 5352
Roupas, Z. 2025, A&A, 702, A208
Roupas, Z. 2026, A&A, 709, A5
Rowan, C., Boekholt, T., Kocsis, B., & Haiman, Z. 2023, MNRAS, 524, 2770
Rowan, C., Whitehead, H., Boekholt, T., Kocsis, B., & Haiman, Z. 2024, MNRAS, 527, 10448
Rowan, C., Whitehead, H., Fabj, G., et al. 2025a, MNRAS, 543, 132
Rowan, C., Whitehead, H., Fabj, G., et al. 2025b, MNRAS, 543, 132
Rowan, C., Whitehead, H., Fabj, G., et al. 2025c, MNRAS, 539, 1501
Rozner, M., Generozov, A., & Perets, H. B. 2023, MNRAS, 521, 866
Rozner, M., & Perets, H. B. 2024, ApJ, 968, 80
Sadowski, A., & Narayan, R. 2016, MNRAS, 456, 3929
Sagynbayeva, S., Li, R., Kuznetsova, A., et al. 2025, ApJ, 987, 216
Samsing, J., MacLeod, M., & Ramirez-Ruiz, E. 2014, ApJ, 784, 71
Samsing, J., & Ramirez-Ruiz, E. 2017, ApJL, 840, L14
Samsing, J., Bartos, I., D'Orazio, D. J., et al. 2022, Natur, 603, 237
Schödel, R., Feldmeier, A., Kunneriath, D., et al. 2014, A&A, 566, 47
Secunda, A., Bellovary, J., Mac Low, M.-M., et al. 2019, ApJ, 878, 85
Secunda, A., Bellovary, J., Mac Low, M.-M., et al. 2019, ApJ, 878, 85
Secunda, A., Bellovary, J., Mac Low, M.-M., et al. 2020, ApJ, 903, 133
Shakura, N. I., & Sunyaev, R. A. 1973, A&A, 24, 337
Shan, X., Yang, H., & Mao, S. 2025, arXiv:2512.19118
Silsbee, K., & Tremaine, S. 2017, ApJ, 836, 39
Sirko, E., & Goodman, J. 2003, MNRAS, 341, 501
Spera, M., Mapelli, M., Giacobbo, N., et al. 2019, MNRAS, 485, 889
Stegmann, J., Olejak, A., & de Mink, S. E. 2025, ApJL, 992, L26

Stephan, A. P., Naoz, S., Ghez, A. M., et al. 2016, MNRAS, 460, 3494
Stone, N. C., Metzger, B. D., & Haiman, Z. 2017, MNRAS, 464, 946
Su, Y., Rowan, C., & Rozner, M. 2025, MNRAS, 543, 1864
Syer, D., Clarke, C. J., & Rees, M. J. 1991, MNRAS, 250, 505
Szolgyen, A., & Kocsis, B. 2018, PhRvL, 121, 101101
Tagawa, H., Haiman, Z., Bartos, I., & Kocsis, B. 2020b, ApJ, 899, 26
Tagawa, H., Haiman, Z., Bartos, I., Kocsis, B., & Omukai, K. 2021a, MNRAS, 507, 3362
Tagawa, H., Haiman, Z., Kimura, S. S., Yesuf, H. M., & Guo, H. 2026a, ApJ, 1006, 121
Tagawa, H., Haiman, Z., & Kocsis, B. 2020c, ApJ, 898, 25
Tagawa, H., Kimura, S. S., Haiman, Z., Perna, R., & Bartos, I. 2023a, ApJ, 950, 13
Tagawa, H., Kimura, S. S., Haiman, Z., Perna, R., & Bartos, I. 2023b, arXiv:2310.18392
Tagawa, H., Kimura, S. S., Haiman, Z., et al. 2022, ApJ, 927, 41
Tagawa, H., Kocsis, B., Haiman, Z., et al. 2021b, ApJL, 907, L20
Tagawa, H., Kocsis, B., Haiman, Z., et al. 2021c, ApJ, 908, 194
Tagawa, H., Rowan, C., Takátsy, J., et al. 2026b, ApJ, 998, 244
Tanikawa, A., Liu, S., Wu, W., Fujii, M. S., & Wang, L. 2026, ApJ, 1003, 80
Tanikawa, A., Yoshida, T., Kinugawa, T., et al. 2022, ApJ, 926, 83
The LIGO Scientific Collaboration, The Virgo Collaboration, & the KAGRA Collaboration 2026a, ApJL, 1004, L22
The LIGO Scientific Collaboration, The Virgo Collaboration, & the KAGRA Collaboration 2026b, ApJL, 1005, L51
Thompson, T. A., Quataert, E., & Murray, N. 2005, ApJ, 630, 167
Tiwari, V. 2024, MNRAS, 527, 298
Tomar, Y., Hopkins, P. F., & Kremer, K. 2026, PhRvD, 113, 063036
Tong, H., Callister, T. A., Fishbach, M., et al. 2025, arXiv:2511.05316
Toyouchi, D., Hotokezaka, K., Inayoshi, K., & Kuiper, R. 2024, MNRAS, 532, 4826
Trani, A. A., Quaini, S., & Colpi, M. 2024, A&A, 683, A135
Vaccaro, M. P., Mapelli, M., Périgois, C., et al. 2024, A&A, 685, A51
Veronesi, N., Rossi, E. M., & van Velzen, S. 2023, MNRAS, 526, 6031
Veronesi, N., Rossi, E. M., van Velzen, S., & Buscicchio, R. 2022, MNRAS, 514, 2092
Veronesi, N., van Velzen, S., & Rossi, E. M. 2025a, MNRAS, 536, 3112
Veronesi, N., van Velzen, S., Rossi, E. M., & Storey-Fisher, K. 2025b, MNRAS, 536, 375
Vijaykumar, A., Farah, A. M., & Fishbach, M. 2026, ApJL, 999, L30
Vitale, S., Mould, M. & Society Of Physicists Interested in Non-Aligned Spins S. 2025, PhRvD, 112, 083015
Wang, M., Ma, Y., Li, H., et al. 2025a, ApJ, 983, 114
Wang, M., Wu, Q., & Ma, Y. 2025b, ApJ, 993, 139
Wang, Y., Zhu, Z., & Lin, D. N. C. 2024, MNRAS, 528, 4958
Wang, Y.-Z., Li, Y.-J., Gao, S.-J., Tang, S.-P., & Fan, Y.-Z. 2026a, SCPMA, 69, 299562
Wang, Z.-Y., Qin, Y., Hu, R.-C., et al. 2026b, A&A, 708, A62
Whitehead, H., Rowan, C., Boekholt, T., & Kocsis, B. 2024a, MNRAS, 531, 4656
Whitehead, H., Rowan, C., Boekholt, T., & Kocsis, B. 2024b, MNRAS, 533, 1766
Whitehead, H., Rowan, C., & Kocsis, B. 2025, MNRAS, 543, 3768
Williamson, A. R., Lange, J., O'Shaughnessy, R., et al. 2017, PhRvD, 96, 124041
Wong, K. W. K., Baibhav, V., & Berti, E. 2019, MNRAS, 488, 5665
Woosley, S. E., & Heger, A. 2021, ApJL, 912, L31
Xu, Y., Valencia, J., Estellés Estrella, H., et al. 2026, PhRvD, 113, 083001
Xue , L., Haiman, Z., Tagawa, H., & Bartos, I. 2026, arXiv:2605.29305
Xue, L., Tagawa, H., Haiman, Z., & Bartos, I. 2025, PhRvD, 112, 063034
Yang, Q., You, Z.-Q., & Fan, X. 2026, PhRvD, 113, 123055
Yang, S.-C., Han, W.-B., Tagawa, H., Li, S., & Zhang, C. 2025, ApJL, 988, L41
Yang, Y., Bartos, I., Haiman, Z., et al. 2019a, ApJ, 876, 122
Yang, Y., Bartos, I., Gayathri, V., et al. 2019b, PhRvL, 123, 181101
Ye, C. S., Fishbach, M., Kremer, K., & Reina-Campos, M. 2026, ApJ, 997, 267
Yelda, S., Ghez, A. M., Lu, J. R., et al. 2014, ApJ, 783, 131
Yu, Q., & Tremaine, S. 2002, MNRAS, 335, 965
Zevin, M., & Bavera, S. S. 2022, ApJ, 933, 86
Zevin, M., Romero-Shaw, I. M., Kremer, K., Thrane, E., & Lasky, P. D. 2021, ApJL, 921, L43
Zhang, S.-R., Wang, Y., Yuan, Y.-F., et al. 2026, ApJ, 998, 171
Zhu, L.-G., & Chen, X. 2025, ApJL, 989, L15
Zwick, L., Takátsy, J., Saini, P., et al. 2025, ApJ, 991, 131